University of Alberta

Effect of Energy Dissipation Rate on Bitumen Droplet Size

by

Scott L. Mussbacher

A thesis submitted to the Faculty of Graduate Studies and Research
in partial fulfillment of the requirements for the degree of

Master of Science
in
Chemical Engineering

Department of Chemical and Materials Engineering

© Scott L. Mussbacher
Fall 2009
Edmonton, Alberta

Permission is hereby granted to the University of Alberta Libraries to reproduce single copies of this thesis and to lend or sell such copies for private, scholarly or scientific research purposes only. Where the thesis is converted to, or otherwise made available in digital form, the University of Alberta will advise potential users of the thesis of these terms.

The author reserves all other publication and other rights in association with the copyright in the thesis and, except as herein before provided, neither the thesis nor any substantial portion thereof may be printed or otherwise reproduced in any material form whatsoever without the author's prior written permission.

Examining Committee

Dr. Tony Yeung, Chemical & Materials Engineering

Dr. Barry Bara, Syncrude Canada Ltd.

Dr. Mike Lipsett, Mechanical Engineering

Dr. Sean Sanders, Chemical & Materials Engineering

Dedication

For Caroline, my wife, who encouraged and motivated me throughout this entire journey. Without her, this may never have been accomplished. Thank you.

For my parents, who have always provided their unconditional support in whatever I choose to do.

And for Alex, who inspires me to better myself each and every day.

Abstract

The extraction of bitumen (heavy oil) from the oil sands is predominantly achieved through a water-based technology. This involves a slurrying process, typically called conditioning, which is categorized into three equally important steps: bitumen-sand liberation, bitumen coalescence, and air-bitumen attachment. Previous studies found that bitumen recovery was dependent upon process variables such as energy dissipation rate, temperature and caustic addition. Correlations between bitumen droplet size and recovery have also been established; however no investigations linking the aforementioned process variables to the resultant bitumen droplet size had been performed. This work investigates the development of a Batch Extraction Unit built specifically for this investigation as well as a study of the bitumen droplet size as a function of the rate of mechanical energy input.

Acknowledgments

Thank you to Dr. Tony Yeung and Dr. Barry Bara for their help in achieving the objectives of this research. As well, I want to thank all the people at the Syncrude Research Facility who helped with my experimentation; in particular Robert Skwarok and Wayne Jansen.

As well, thank you to NSERC, Syncrude Canada Ltd., and the J. Gordon Koplin Foundation for the financial assistance provided for this research.

Table of Contents

Chapter 1	Introduction	1
1.1	Oil Sands	1
1.2	Oil Sand Extraction	1
1.3	Factors Influencing Bitumen Recovery	3
1.4	Present Study	4
References		6
Chapter 2	Literature Review	7
2.1	Introduction	7
2.2	Definitions	7
2.2.1	Sauter Mean Diameter, d_{32}	7
2.2.2	Power Number	10
2.2.3	Average and Local Dissipation Energy	11
2.2.4	Maximum Energy Dissipation Rate	13
2.3	Droplet Breakup and Coalescence	13
2.3.1	Breakup Mechanisms	13
2.3.2	Coalescence Mechanisms	14
2.3.3	Range of Concentration for Coalescence	15
2.3.4	Droplet Size Theory	16
2.3.5	Time for Drop Size Stability	20
2.4	Tank Geometry	22
2.4.1	Tank Bottom	22
2.4.2	Impellers	23
2.4.3	Liquid Height	26
2.4.4	Impeller Clearance	26
2.5	Literature Review Conclusions	27
References		28
Chapter 3	Experimental Design	31

3.1	Introduction	31
3.2	Experimental Setup	31
3.2.1	The Mixing Tank	31
3.2.2	Mixing Tank Lid	33
3.2.3	Motor Mixer Device	34
3.2.4	Data Collection/Analysis Instrumentation	36
3.3	Equipment Calibration	36
3.3.1	Torque Transducer Calibration	37
3.3.2	Power Number Calibration	37
3.3.3	Minimum Calculable Droplet Size	41
3.3.4	Software Calibration	41
3.3.5	Camera Calibration	46
3.4	Experimental Fluids	48
3.4.1	Bitumen Selection	48
3.4.2	Continuous Phase (Water) Selection	53
3.4.2.1	Water Selection: Theoretical Considerations	54
3.4.2.2	Water Selection: Experimental Considerations	55
3.5	Experimental Operations	57
3.5.1	Experimental Procedure	57
3.5.2	Analysis Procedure	58
3.6	Conclusions	61
References		62
Chapter 4	Results and Discussion	64
4.1	Introduction	64
4.2	Model Oils	64
4.2.1	Model Oil Selection	64
4.2.2	Model Oil Results	65
4.2.3	Model Oil Discussion and Validation of Experimental Setup	69
4.3	Bitumen Experiments	69

4.3.1	Effect of Varying Agitation Device	69
4.3.2	Power Law Relationship	70
4.4	Analysis of Potential Errors	73
4.4.1	Error in ε_{max} Calculation Related to Power Law Relationship Deviation	73
4.4.2	Effect of Viscosity Variation on Power Law Relationship	76
4.4.3	Effects of Water Chemistry on Experimental Power Law Relationship	76
4.4.4	Effect of Viscosity on ε_{max}	76
4.5	Conclusions	79
Chapter 5	Conclusions and Recommendations	80
5.1	Introduction	80
5.2	Objective 1: Experimental Design and Calibration	80
5.3	Objective 2: Dmax vs ε_{max} Relationship	81
5.4	Future Work	81
Appendix	Sample Calculation	82

List of Figures

Figure 1.1	Map of Alberta's Oil Sand Deposits	2
Figure 2.1	d_{max} vs $\boldsymbol{\varepsilon_{max}}$ using data from Arai (1977) for 6 fluid viscosities	21
Figure 2.2	Flow Patterns Created by Axial Impellers	24
Figure 2.3	Flow Patterns Created by Radial Impellers	24
Figure 3.1	Experimental Apparatus	32
Figure 3.2A	Photo of the Hydrofoil	35
Figure 3.2B	Photo of the Rushton Turbine	35
Figure 3.3	Power Number of Hydrofoil	39
Figure 3.4	Power Number of Rushton Turbine	40
Figure 3.5	Circles Created in Paint for Software Analysis	42
Figure 3.6	DaVis Analyzed Circles	43
Figure 3.7	Percent Error between Actual Circle Diameter and DaVis Circle Diameter	44
Figure 3.8	Global Composites	45
Figure 3.9	Droplet Distribution vs Frame Height	47
Figure 3.10	Frame Height as a function of Camera Distance from Tank	49
Figure 3.11	Comparison between Current Study Analysis and Coanda	50
Figure 3.12	Temperature vs Bitumen Viscosity	52
Figure 3.13	Electrical Double Layer around Bitumen Droplets	56
Figure 4.1	Viscosity vs Temperature for Toluene diluted Bitumen	66
Figure 4.2	Maximum Droplet Size vs Maximum Energy Dissipation Rate for Bitumen/Toluene Blend	67
Figure 4.3	Comparison of Toluene Diluted Bitumen Power Law Exponent to Arai (1977)	68

Figure 4.4	ε_{max} vs impeller speed for Hydrofoil and Rushton Turbine	71
Figure 4.5	d_{max} vs ε_{max} for Atmospheric Topped Bitumen	72
Figure 4.6	Comparison of Atmospheric Topped Bitumen Power Law Exponent to Arai (1977)	74
Figure 4.7	Temperature Profile of Typical Experiment	77
Figure 4.8	Maximum Droplet Size vs Bitumen Viscosity	78
Figure A.1	Example Photograph of for Analysis by DaVis	84
Figure A.2	Figure A.2: Maximum Droplet Size vs Time for Hydrofoil @ 503 RPM	86

List of Tables

Table 2.1	Dilute System Concentrations in Other Studies	16
Table 2.2	Literature Power Numbers for Hydrofoil	25
Table 2.3	Literature Power Numbers for Rushton Turbine	25
Table 3.1	Impeller Specifications	36
Table 3.2	Coanda Results for Glass Beads	46
Table 3.3	Atmospheric Topped Bitumen Characteristics	53
Table 3.4	Tap Water Quality Analysis	54
Table 3.5	Geometry Comparison	60
Table 4.1	Power Law Exponent Error as a Result of Rushton Turbine and Hydrofoil Constant Error	75
Table A.1	Table A.1: Illustration of DaVis Software Output	85

Nomenclature

A	constant	
b	moment arm	(m)
C	impeller clearance	(m)
d	droplet diameter,	(m)
d_{32}	Sauter Mean Diameter,	(m)
d_{max}	maximum Droplet Size	(m)
D	impeller Diameter	(m)
E(k)	energy spectrum function	
k		
L	characteristic length of eddies	(m)
n_i	number of droplets of size i	
n_p	number of droplets per unit volume	($1/m^3$)
N	rotational rate	(1/s)
Np	power number	
P	power	(kg m^2/s^3 or W)
Re	Reynolds Number	
SA	surface area	(m^2)
t_c	time of droplet contact	(s)
t_d	time for film drainage	(s)
T	tank diameter	(m)
T_q	torque	(N·m)
V	root mean square of the fluctuating velocities	(m/s)
V	volume	(m^3)

Greek

Φ	volume fraction of dispersed phase	
ξ	collision frequency	($1/m^3s$)
τ_c	shear stress	(N/m^2)

τ_d	resistive stress due to interfacial tension	(N/m^2)
τ_s	resistive stress due to viscosity	(N/m^2)
η	Kolmogoroff's microscale	(m)
β	Kolmogoroff constant	
σ	interfacial tension	(N/m)
μ	absolute viscosity	(kg/m·s)
ρ	density	(kg/m3)
ε	local energy dissipation rate	(W/kg)
ε_{max}	maximum energy dissipation rate	(W/kg)
$\bar{\varepsilon}$	average energy dissipation rate	(W/kg)
λ_c	coalescence efficiency	
Γ	coalescence frequency	
ω	constant	

Subscripts

c	continuous phase
d	dispersed phase
max	maximum
TOT	total

Chapter 1
Introduction

1.1 Oil Sands

Oil sands are comprised of bitumen, clays, silica sand, and water. Bitumen is a highly viscous oil that can be found in the Athabasca oil sands deposit located primarily in Northern Alberta. An illustration of the Albertan oil sands deposits can be seen in **Figure 1.1**. The Athabasca oil sands deposit contains approximately 1.7 trillion barrels of unproven reserves and 178 billion barrels of proven reserves which represents nearly 15% of the world's proven recoverable oil deposits (Alberta Government). Currently, Canadian oil sands production is approximately one million barrels a day, constituting 35% of Canada's total daily oil production (Alberta Government). The Canadian Association of Petroleum Producers (Whiteside, CAPP) expects that by 2015 daily oil sands production will increase 250% to 3.5 million barrels per day. Additionally, by 2020, CAPP expects that over 80% of Canada's oil production will originate from the oil sands in Northern Alberta (CAPP).

Recovery rates of bitumen from oil sand are already typically over 90% however even marginal improvement can lead to vast increases in profit. For example, the Syncrude Project's current design production capacity is 350,000 barrels per calendar day. By improving the recovery rate by only 1%, an additional fifty million dollars per year of net income could be generated (Canadian Oil Sands Trust). Therefore, it is imperative that sustained investigation and research be performed in this field to maximize the recovery rates of the bitumen. This chapter will give a brief overview of oil sands extraction, the factors influencing bitumen recovery, and conclude by introducing the objectives and scope of this investigation.

1.2 Oil Sand Extraction

In 1929, Dr. Karl Clark patented a process of separating the heavy oil contained in the oil sands (Heritage Community Foundation). The process mining

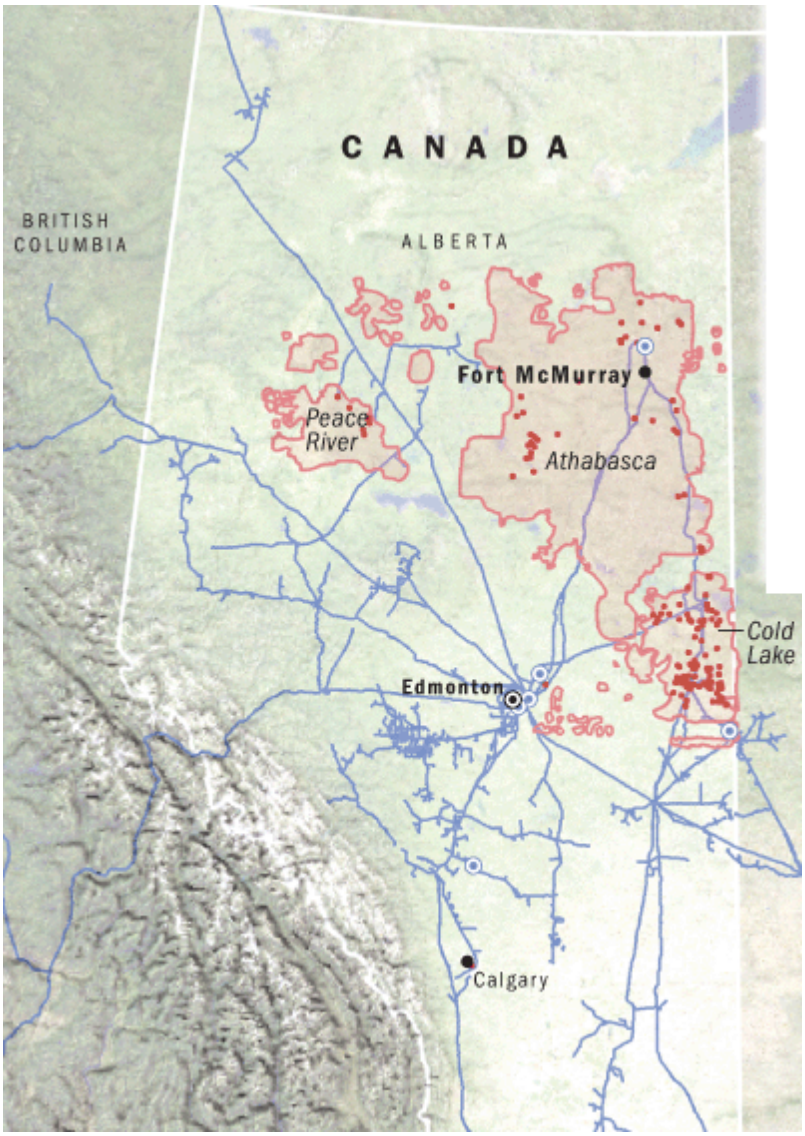

Figure 1.1 – Alberta Oil Sands Deposits

operations. Recently, several in-situ operations have been established; however, the three largest oil sands operations continue to use surface mining methods.

In a typical surface mining operation, gigantic shovels and trucks are used to mine the raw oil sand. The oil sand is then fed into a pipeline where it is combined with water to form a slurry; chemicals may be added to the slurry to aid in its processing. The slurry is then pumped from the mine to the base plant in a process called hydrotransport. During this transport, bitumen is separated from the sand and aerated. Upon arriving at the plant, the slurry is fed into gravity separation vessels called the Primary Separation Vessels where the bitumen droplets float to the top. The floated bitumen is recovered off the top using a skimmer and sent on for further processing.

1.3 Factors Influencing Bitumen Recovery

The ultimate goal of this extraction process is to maximize the recovery of bitumen from the oil sand. In extraction, there are three major steps that the bitumen must undergo to be recovered.

1) *Oil Sand Break-Up and Bitumen Liberation* - The matrix of bitumen and sand is broken via agitation and the bitumen is released from the sand grains. This step occurs primarily during hydrotransport. Energy dissipation rates (e.g. through turbulence) during this process impact the size of bitumen droplets and the extent of bitumen separation from the sand within the pipeline.
2) *Bitumen Coalescence* - After liberation, the bitumen droplets may coalesce to form larger droplets. Again, this step primarily occurs during hydrotransport. There are many different factors that can affect the rate and extent of coalescence within the system; they include initial droplet size, temperature (i.e. bitumen viscosity), water chemistry, surface chemistry, quiescent zones and turbulence, and concentration.

3) *Bitumen Aeration* - A step occurring concurrently with the above steps is air attachment to the bitumen. Factors affecting this process include bitumen droplet and air bubble size, water chemistry, and bitumen surface chemistry.

Ultimately, these three mechanisms contribute to the final bitumen droplet size and density. The size and density of the aerated bitumen droplets are of critical importance in the gravity separation process. By increasing the droplet size and decreasing the density, the rise velocity of the bitumen droplets will increase, thereby improving recovery efficiency within the Primary Separation Vessel. Therefore, the bitumen droplet size and density are important factors influencing bitumen recovery in the primary separation vessel.

The study of bitumen suspended in water is essentially an investigation in liquid-liquid dispersions. A significant amount of research in liquid dispersions has been performed in the past fifty years; however, investigations with highly viscous dispersed fluids, such as bitumen, are rare. The present study will serve to improve understanding of bitumen systems as well as dispersions involving highly viscous droplets.

1.4 Present Study

The purpose of this investigation is to increase the fundamental knowledge of the effect of turbulence on bitumen droplet size. From this, an enhanced understanding of bitumen dispersions can aid future studies aimed at investigating the effects on the industrial process. To achieve this goal, the following objectives are to be accomplished:

1) A batch extraction unit, capable of monitoring the bitumen droplet size in-situ, is to be designed and built; the equipment is to be calibrated and results from controlled experiments are to be compared with other liquid-liquid dispersion studies to validate the present experimental apparatus and

2) A relationship between bitumen droplet size and energy dissipation rate is to be established

References

Alberta Government, "What is Oil Sands." Energy – Government of Alberta. http://www.energy.gov.ab.ca/100.asp

Canadian Association of Petroleum Producers (CAPP), "Canadian Crude Oil Production and Supply Forecast 2005-2015." Canadian Association of Petroleum Producers (CAPP). http://www.capp.ca/raw.asp?x=1&dt=NTV&e=PDF&dn=89357

Canadian Oil Sands Trust, "Annual Report 2008." Canadian Oil Sands Trust. http://www.cos-trust.com/Theme/COS/files/FinancialReports/COS_AR_2008_FINAL.pdf

Heritage Community Foundation, "Alberta's Heroes of Resource Development." Alberta Online Encyclopedia. http://www.abheritage.ca/abresources/history/history_heroes_clark.html

Whiteside, J., "CAPP Releases 2006 Crude Oil Forecast." Canadian Association of Petroleum Producers (CAPP). http://www.capp.ca/default.asp?V_DOC_ID=1169

Chapter 2
Literature Review

2.1 Introduction

Immiscible liquid-liquid dispersions occur frequently in industrial processes. They are encountered in industries such as pharmaceuticals, food processing, and petroleum recovery. The importance of this process has provoked an extensive amount of investigation into understanding of the mechanics and characteristics of dispersions. One of the most important factors determining the characteristics of a dispersion is the level of turbulence within the system. Other important factors include the mechanics of droplet breakup and coalescence and the geometry of the mixing system. Each of these factors influences the effects of the others; therefore slightly different design parameters can cause significant changes in the characteristics of the dispersed phase.

Extensive research investigating the aforementioned factors has been performed. Typically, the research has focused on the extent and characterization of the suspended liquid. This chapter is a review of the work performed to date. It will begin by defining several important concepts required in the field. Next, a synopsis of the mechanisms of droplet break up and formation will be given, followed by a scheme for predicting droplet sizes. It will conclude by giving a summary of the characteristics of the mixing apparatus typically used when investigating liquid-liquid dispersions.

2.2 Definitions

This section is an overview of important terms and properties used to define and characterize liquid-liquid dispersions. It will cover several concepts including the definitions of several measures of “mean” droplet diameter and energy dissipation rate.

2.2.1 Sauter Mean Diameter, d_{32}

There are numerous ways to define the droplet size distribution within an

immiscible liquid-liquid dispersion. The most comprehensive method is to report the distribution as a graph illustrating the frequency of occurrence of each drop size. However, comparing and reporting distributions using this technique can be challenging. A different method of describing the droplet size distribution is to report one of a variety of "mean" diameters. Some examples of these are:

1) *d[v,10]* - 10% of all droplets, by volume, are smaller than d[v,10],
2) *d[v,50]* - 50% of all droplets, by volume, are smaller than d[v,50],
3) *d[v,90]* - 90% of all droplets, by volume, are smaller than d[v,90], and
4) d_{32} - Sauter mean diameter (see below)

Of these "mean" diameters, the Sauter mean diameter, d_{32}, is typically regarded as the most valuable characteristic for determining the extent of dispersion in a liquid-liquid mixture (Leng and Calabrese, 2004). This is because it relates the interfacial area to the volume of the dispersed phase. The Sauter Mean Diameter is defined as:

$$d_{32} = \frac{\sum_i n_i d_i^3}{\sum_i n_i d_i^2} \tag{2-1}$$

where d is the droplet diameter and n_i is the number of droplets of size d_i.

The following derivation shows how the surface area and volume of the droplets are incorporated into the Sauter mean diameter. The surface area, SA, and volume, V_d, of a single sphere (i.e. a droplet) are:

$$SA = \pi d^2 \tag{2-2}$$

$$V_d = \frac{\pi d^3}{6} \tag{2-3}$$

Using these equations, the total surface area, SA_{TOT}, and total volume, V_{TOT}, of the entire dispersed phase (assuming all droplets are perfect spheres) is:

$$SA_{TOT} = \sum_i n_i d_i^2 \pi \tag{2-4}$$

$$V_{TOT} = \frac{\sum_i n_i d_i^3 \pi}{6} \tag{2-5}$$

As such, the ratio of the total surface area to the total fluid volume is:

$$a = \frac{SA_{TOT}}{V_{TOT}} = 6\phi \frac{\sum_i n_i d_i^2 \pi}{\sum_i n_i d_i^3 \pi} \tag{2-6}$$

where Φ is the dispersed volume phase fraction and a is the total interfacial area per unit volume.

Simplifying equation (2-6) by inserting equation (2-1) gives:

$$a = \frac{6\phi}{d_{32}} \tag{2-7}$$

$$d_{32} = \frac{6\phi}{a} \tag{2-8}$$

Therefore, it can be seen that the Sauter mean diameter, d_{32}, is representative of the specific surface area (i.e. total interfacial area per unit volume) of the suspension. It is important to note that all droplets are considered perfectly spherical using this approach.

Many authors (Brown and Pitt, 1972; Coulaloglou and Tavlarides, 1976; Calabrese et al., 1986; Nishikawa et al., 1987; Berkman and Calabreses, 1988; Zhou, 1997) have suggested a relationship between d_{32} and the maximum droplet size, d_{max} in the form:

$$d_{32} = constant \times d_{\max} \tag{2-9}$$

Estimates by the aforementioned authors for the constant in equation (2-9) vary between 0.38 and 0.70. However, Zhou et al. (1998) discovered a linear relationship between the constant and ND^2. This corresponds to the Reynolds number in a mixing tank (Marshall and Bakker, 2004) where the Reynolds number is

$$\mathrm{Re} = \frac{\rho N D^2}{\mu}$$

Therefore, Zhou found that the constant in equation (2-9) exhibits a linear relationship with the Reynolds number.

2.2.2 Power Number

The power number, N_P, is a dimensionless parameter relating the impeller speed to the power transferred to the fluid. In fully turbulent flow (i.e. a Reynolds number greater than 2000), the N_P is constant for a given impeller size and tank geometry. Rushton et al. (1950A) showed that the power number can vary widely between impellers of different types and sizes. The following equation can be used to calculate the power number for any mixing operation using an impeller:

$$N_P = \frac{2\pi T_q}{\rho_c N^2 D^5} = \frac{P}{\rho_c N^3 D^5} \tag{2-10}$$

where T_q is the torque (N·m), P is the power input (W), ρ_c is the continuous phase density (kg/m^3), N is the rotational speed of the impeller (rev/s), and D is the impeller diameter (m).

The power number is essentially the drag coefficient for the impeller (Hemrajani and Tatterson, 2004). It is a representation of the ability of an impeller to dissipate energy into the system. Impeller specific information regarding N_P can be found in **Section 2.4.2**.

2.2.3 Average and Local Energy Dissipation

Energy dissipation into a mixing tank can be achieved in a number of ways. In simple liquid-liquid dispersions where reactions are not taking place, it is assumed that the only energy transferred to the fluid is via mechanical agitation (i.e. from the impeller).

The rate of energy input into the system can be expressed as the time and space averaged energy dissipation rate, $\bar{\varepsilon}$ (W/kg). It can be calculated using the following equation:

$$\bar{\varepsilon} = \frac{P}{\rho_c V_T} \tag{2-11}$$

where V_T is the volume of the tank.

The use of $\bar{\varepsilon}$ to represent energy dissipation into the tank is not indicative of the turbulence or mixing intensity within the system. An alternate measure of the energy dissipation rate is via the local dissipation parameter, ε (W/kg or m^2/s^3). Batchelor (1953) estimated the following equation for ε:

$$\varepsilon = A\frac{v^3}{L} \tag{2-12}$$

where A is an empirical constant on the order unity, ν is the root mean square (rms) of the fluctuating velocities, and L is the characteristic length of the large

eddies. It should be noted that the turbulent flow pattern is assumed to be isotropic when using the rms of the fluctuating velocities (see isotropy discussion in **Section 2.3.4**).

The fluctuating velocity at a specific point within a system can be measured using a laser Doppler anemometer. However in the absence of such measurements, an alternative method must be used. Several authors have gathered empirical data showing that fluctuating velocity is proportional to ND (Bertrand et al., 1980; Ranada and Joshi, 1989; Dyster, 1993). Additionally, the characteristic length of the large eddies can be assumed to be proportional to the impeller diameter, D (Brodkey, 1975). Therefore, substituting these relationships into equation (2-12) gives:

$$\varepsilon = A\frac{(C_1 ND)^3}{C_2 D} \tag{2-13}$$

where C_1 and C_2 are dimensionless constants.

Combining the constants and simplifying, the local energy dissipation rate for any point within the system becomes:

$$\varepsilon = C_3 N^3 D^2 \tag{2-14}$$

where both C_3 and, subsequently, ε are functions of position and the empirical constant, A, is on the order unity.

Therefore, the local energy dissipation rate can be predicted for any point assuming the constant C_3 is known. Values for C_3 have been calculated by Zhou (1997) and are on the order of 1 to 100 depending on the tank geometry. This technique of calculating the energy dissipation rate is much more representative of the actual mixing conditions within the tank. Okamoto et al. (1981) showed that the local dissipation rate could vary by up to 50 times between two locations within the tank at any given time. Therefore, when investigating the forces

experienced by each droplet within a tank, the local energy dissipation rates should be considered.

2.2.4 Maximum Energy Dissipation Rate

At certain locations within a system, the energy dissipation rate reaches a maximum. It is important to consider this maximum energy dissipation rate, ε_{max}, when investigating droplet breakup because this corresponds to the highest shear rate that the liquid drop will experience. Therefore, the ε_{max} is critical in determining the equilibrium drop size within the system.

Zhou (1998) determined the values of C_3 in equation 2-14 in order to calculate ε_{max} for a variety of tank geometries and impeller types. For a Hydrofoil, the values of C_3 ranged from 0.467 to 1.22 while values for a Rushton Turbine varied from 9.75 to 19.9.

2.3 Droplet Breakup & Coalescence

Energy dissipation rates play an important role in determining the droplet sizes of a dispersed fluid. The droplet size is determined by two opposing mechanisms: droplet breakup and coalescence. Equilibrium between droplet breakup and coalescence will eventually occur and an equilibrium droplet size distribution is defined. The following section will discuss breakup, coalescence, and the balance between the two.

2.3.1 Breakup Mechanisms

Current understanding of droplet breakup was proposed by Hinze in 1955. He proposed three basic types of droplet deformation and breakup:

1) *Lenticular Deformation and Breakup*. Rotational flow patterns cause the droplet to become a flattened ellipsoid. Significant differences in density between the two fluids are required for the centrifugal forces to bring about droplet breakup. Droplet

impacts with the walls, impeller blades, and baffles typically cause this type of deformation.

2) *Cigar-Shaped Deformation and Breakup.* The droplet is elongated into a cylinder whereby droplets may break off at either end. This type of droplet breakup typically occurs due to uniform shear and is especially important in liquid-liquid dispersions.

3) *Bulgy Deformation and Breakup.* Local perturbations near the edge of the droplet cause bulges on the surface. Strong disturbances in turbulent flow may cause small daughter droplets to break off.

Each mechanism requires different forces to precipitate deformation and breakup. During mixing, any combinations of these mechanisms can occur. The ratio of the continuous and dispersed phase viscosities is an important factor in the extent of deformation in all three regimes.

2.3.2 Coalescence Mechanisms

Coalescence occurs when two or more dispersed droplets collide and combine to form a single droplet. Coalescence is a multi step process in which a series of probabilities dictate the rate of coalescence. The first requirement for coalescence is for two droplets to collide. The collision frequency, ξ_c, is the number of collisions per unit volume per unit second (e.g. no. m^{-3} s^{-1}). Based on Kolmogoroff's theory for equal sized droplets in isotropic turbulence:

$$\xi_c \propto d^{7/3} \varepsilon^{1/3} n_P^2 \qquad (2\text{-}15)$$

where n_p is the number of drops per unit volume.

Upon collision, the probability that the two droplets will coalesce is known as the coalescence efficiency, λ_c. The coalescence efficiency is dependent

upon the length of time in which the droplets are in contact, t_c, and the length of time required for film drainage, t_d (Leng and Calabrese, 2004):

$$\lambda_c \propto \exp(-t_d / t_c) \tag{2-16}$$

Furthermore, t_d is dependent upon the mobility of the film, liquid viscosity, interfacial tension, force of collision, and presence of surfactants. Finally, the coalescence frequency, Γ, is a defined as the product of the collision frequency and the coalescence efficiency (Leng and Calabrese, 2004):

$$\Gamma = \lambda_c \xi_c \tag{2-17}$$

Due to the inability to accurately quantify all hydrodynamic and physicochemical forces involved in film drainage, the coalescence efficiency and frequency are difficult to determine.

2.3.3 Range of Concentration for Coalescence

The collision frequency of the droplets is highly dependant on the concentration of the dispersed liquid in an immiscible liquid-liquid mixture. This is illustrated in equation (2-15). Therefore, in very dilute systems, the collision frequency is essentially zero and, consequently, coalescence frequency also becomes insignificant. In this case, coalescence can be neglected and droplet breakup can be considered to be the sole mechanism dictating the final droplet size distribution. **Table 2.1** summarizes the concentration of dispersed liquids in experiments where coalescence was assumed to be negligible.

Table 2.1: Dilute System Concentrations in Other Studies

Authors	Year	Φ	Continuous Liquid	Dispersed Liquid
Chen and Middleman	1967	0.005	DI Water	Various
Calabrese et al.	1986	0.0015	DI Water	Several Silicone Oils
Baldyga et al.	2001	0.01	Water	Chlorobenzene
Leng and Calabrese	2004	0.05	-	-
Nienow	2004	0.01	DI Water	Silicone Oil

2.3.4 Droplet Size Theory

The difficulty in developing a predictive model for droplet size in a mixing operation is determining the balance between droplet breakup and coalescence. In any predictive model, changes of process variables can easily influence the flow patterns and mixing, thereby altering the parameters critical to its success. Therefore, as a starting point, a simplified model is preferred.

The most difficult aspect in determining the equilibrium droplet size distribution is the modeling of coalescence. By neglecting droplet coalescence, the problem of predicting the final droplet size is significantly simplified. Disregarding coalescence is practical for systems in which the collision frequency and/or the coalescence frequency is extremely low (see equation (2-17)). Therefore in experiments with dispersed fluid concentrations on the order of those seen in **Table 2.1**, only droplet breakup needs to be considered. Using the arguments of Kolmogoroff (1949) and Hinze (1955), a relatively simplistic model for droplet breakup in a dilute, non-coalescing turbulent system can be developed as outlined in Leng and Calabrese (2004).

Their arguments state that a droplet will break apart if the shear stresses acting on the droplet are greater than the stresses holding it together. The balance between these stresses can be seen in the following equation:

$$\tau_c = \tau_s + \tau_d \qquad (2\text{-}18)$$

where τ_c is the shear stress on the droplet due to the surrounding turbulent flow field surrounding it, τ_s is the resistive stress due to interfacial tension, and τ_d is the resistive viscous stress within the drop.

When the disruptive forces are in balance with the cohesive forces, the maximum stable droplet size, d_{max}, will occur. In most mixing vessels, d_{max} is smaller than the turbulent macroscale eddies but larger than the Kolmogoroff microscale, η. The Kolmogoroff microscale is defined as:

$$\eta = \left(\frac{\nu^3}{\varepsilon} \right)^{1/4} \tag{2-19}$$

The continuous fluid exerts the shear stress, τ_c, on the droplets. The turbulent conditions of the continuous phase can described by the energy spectrum function, E(k) where k is the wave number (i.e. inverse eddy size). The turbulent energy per unit mass can be represented by E(k)dk as influenced by fluctuations of the wave number from k to k + dk. As such, the shear stress on the droplet, τ_c, is given by:

$$\tau_c = \rho_c \int_{1/d}^{\infty} E(k) dk \tag{2-20}$$

where the integration limits are from 1/d to infinity since only energy fluctuations smaller in scale than 1/d cause potential droplet breakup; larger fluctuations only cause droplet deformation (Leng and Calabrese, 2004).

The droplet size distribution is determined primarily in the inertial subrange. To develop an expression for E(k), an assumption must be made. Kolmogoroff's theory of local isotropy (Kolmogoroff 1941a,b) states that eddies in the inertial subrange are locally isotropic. More recently, Zhou (1998) confirmed this theory using a laser Doppler anemometer. Zhou measured the three fluctuating velocities (in the z, r, and θ directions) in the region of maximum turbulence. He found that they are essentially equal thereby showing that the

turbulence was isotropic. Therefore, according to Kolmogoroff's theory, and assuming local isotropy, E(k) can be given by:

$$E(k) = \beta_k \varepsilon^{2/3} k^{-5/3} \qquad (L >> d >> \eta) \tag{2-21}$$

where β_k is the Kolmogoroff constant (~3/2).

Inserting equation (2-21) into equation (2-20), the shear stress on a droplet can be expressed as:

$$\tau_c \approx \rho_c \varepsilon^{2/3} d^{2/3} \qquad (L >> d >> \eta) \tag{2-22}$$

The resistive stress, due to the interfacial tension of the droplet, can be expressed as:

$$\tau_s \approx \sigma / d \tag{2-23}$$

where σ is the interfacial tension (N/m).

The resistive stress due to viscosity was assumed by Hinze (1955) to be proportional to the characteristic velocity in the drop, $\sqrt{\tau_c / \rho_d}$. The viscous stress within the droplet is:

$$\tau_d \approx \mu_d \frac{\sqrt{\tau_c / \rho_d}}{d} \tag{2-24}$$

where μ_d is the droplet viscosity and ρ_d is the droplet density. Equation (2-24) can be seen as an approximation of Newton's law of viscosity: $\tau = \mu(du/dy)$.

Finally, equations (2-22), (2-23), and (2-24) can be substituted into equation (2-18) to find the maximum droplet size associated with the maximum energy dissipation, ε_{max}:

$$\frac{\rho_c \varepsilon_{\max}^{2/3} d_{\max}^{5/3}}{\sigma} = C_4 \left[1 + C_5 \left(\frac{\rho_c}{\rho_d} \right)^{1/2} \frac{\mu_d \left(\varepsilon_{\max} d_{\max} \right)^{1/3}}{\sigma} \right] \qquad (2\text{-}25)$$

where C_4 and C_5 are constants.

This equation is only valid for droplets that have passed through the region of maximum energy dissipation. The time required for all droplets to pass through this region is discussed later in this chapter (see **Section 2.3.5**). Further simplification can be performed on equation (2-25) by considering only the dominant force which resists droplet breakup. Two cases emerge:

1) *Interfacial Tension-dominated Resistance (ITR).* The force resisting droplet breakup is dictated primarily by interfacial tension. i.e.:

$$\tau_s >> \tau_d \qquad \text{and} \qquad C_5 \left(\frac{\rho_c}{\rho_d} \right)^{1/2} \frac{\mu_d \left(\varepsilon_{\max} d_{\max} \right)^{1/3}}{\sigma} << 1$$

In this case, equation (2-25) subsequently simplifies to:

$$d_{\max} = C_4 \left(\frac{\sigma}{\rho_c} \right)^{3/5} \varepsilon_{\max}^{-2/5} \qquad (2\text{-}26)$$

where C_4 is on the order of unity (Hinze, 1955)

2) *Viscosity-dominated Resistance (VR).* The fluid viscosity is the primary factor governing the restoring force within the droplet. i.e.

$$\tau_s << \tau_d \qquad \text{and} \qquad C_5 \left(\frac{\rho_c}{\rho_d} \right)^{1/2} \frac{\mu_d \left(\varepsilon_{\max} d_{\max} \right)^{1/3}}{\sigma} >> 1$$

In this case, equation (2-25) subsequently simplifies to:

$$d_{\max} = C_6 \left(\rho_c \rho_d\right)^{-3/8} \mu_d^{3/4} \varepsilon_{\max}^{-1/4} \tag{2-27}$$

In both cases, there is in a monotonically decreasing relationship between the maximum stable droplet size and the maximum energy dissipation rate. Comparing the two expressions (equations 2-26 and 2-27), an increasing ε_{max} causes a faster d_{max} decay in the ITR case than the VR case as seen in the difference in the power law exponents of –2/5 (-0.40) to –1/4 (-0.25) respectively.

This finding is supported by the data of Arai (1977). **Figure 2.1** illustrates the response of d_{max} to a change in ε_{max} for six fluids of varying viscosity as performed by Arai. Originally, Arai reported the response of d_{max} to a change in RPM within the system. In order to plot ε_{max}, equation (2-14) was used to convert the RPM values into the maximum energy dissipation rate. Additionally, the constant was assumed to be the average of the values determined by Zhou (1998) as discussed in **Section 2.2.4**. The six fluids were graphed and their power law equations were found using excel. The ITR system (0.78 cp fluid) exhibits a power law exponent of –0.417 which is very similar to the value of –0.40 derived in equation (2-26). Additionally, Arai's VR dominated system (1500 cp fluid) produced a power law exponent of –0.254, similar to the exponent of –0.25 derived in equation (2-27). These two systems exhibited percent errors in their power law exponents of 4.3% and 1.5% respectively, indicating that the assumptions made in deriving the theory are likely to be valid.

2.3.5 Time for Drop Size Stability

It is generally agreed that equilibrium between droplet breakup and coalescence occurs after certain mixing time. Typically, this is determined graphically by plotting the chosen diameter (e.g. d_{32}, d_{max}, or mean diameter) as a function of time. Traditionally, authors such as Chen and Middleman (1967) and Arai et al. (1977) proposed an equilibrium time of 30 and 40 minutes respectively. Perhaps, due to increased precision in droplet size measurements, this mixing

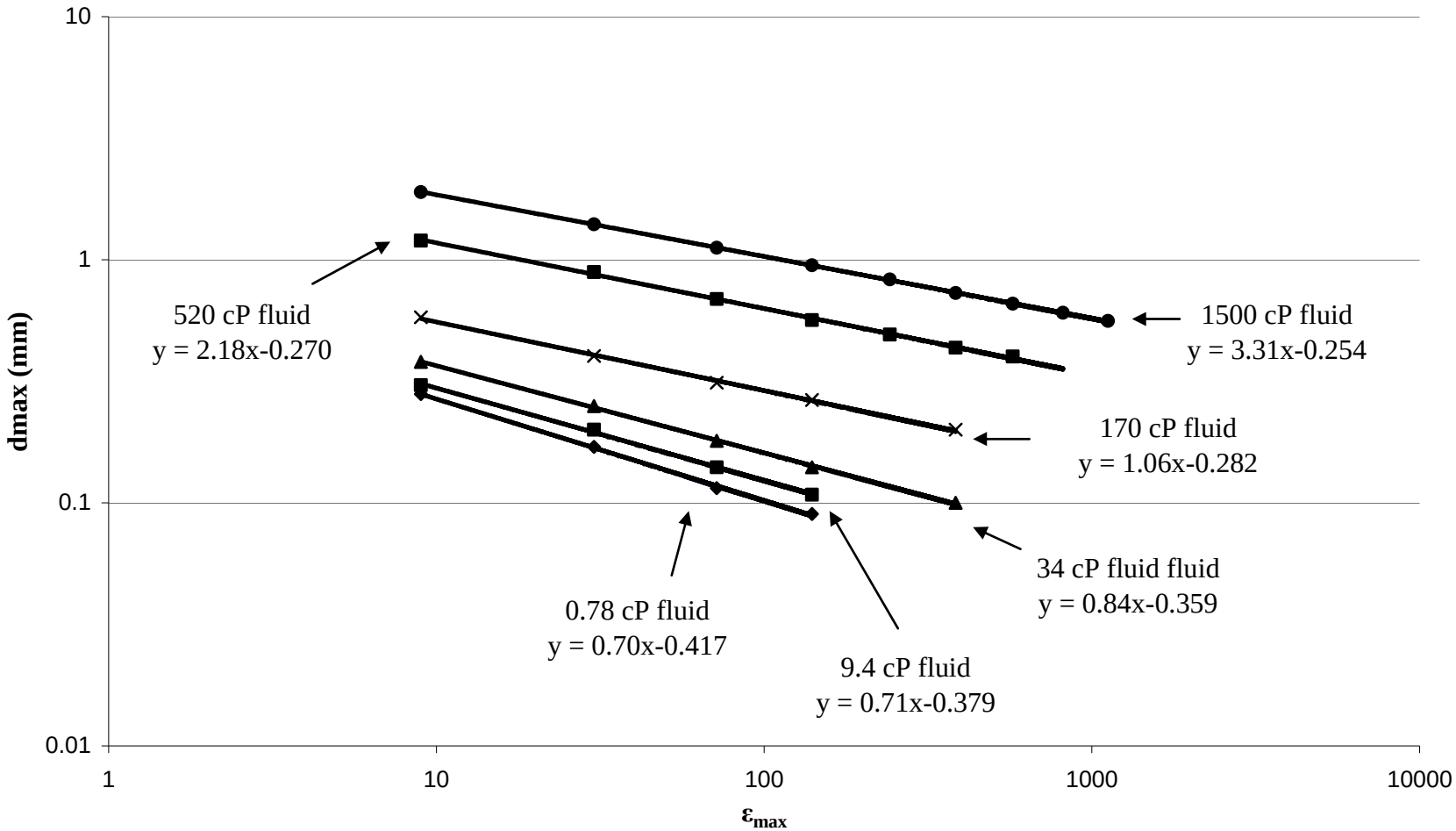

Figure 2.1 dmax vs εmax using data from Arai (1977) for 6 fluid viscosities

time has increased over the years. Calabrese et al. (1986) cited an equilibration time of 1 hour for low viscosity dispersed fluids and 2 hours for high viscosity dispersed fluids. Recently, Pacek et al. (1998), Zhou and Kresta (1998), and Baldyga et al. (2001) have shown that the time for a constant maximum drop size to develop is 180 to 200 minutes. As well, Pacek et al. (1999) determined that the length of time required to reach equilibrium was dependant upon the type of impeller used for agitation. They reached this conclusion by showing that the equilibrium time for a hydrofoil was ~1 hour while a Ruston Turbine was ~3 hours.

2.4 Tank Geometry

The geometry of a tank has a significant effect upon flow patterns and energy dissipation rates within a system. When comparing and examining different geometries, complications arise due to the interactions between several geometric parameters (e.g. tank diameter (T) and impeller diameter (D), D and impeller clearance (C), and C and T). The final section of this chapter will investigate the experimental design of other liquid-liquid dispersion investigations. The goal is to examine the tank parameters required for adequate suspension and agitation of bitumen-water dispersions.

2.4.1 Tank Bottom

The bottom of a mixing tank has a large influence on the flow patterns within the tank and the dispersed droplet size distribution in liquid-liquid operations (Zhou and Kresta, 1998). Therefore, it is extremely important to select the proper tank bottom such that adequate mixing of the components is achieved.

Leng and Calabrese (2004) recommended against the use of flat or cone bottomed tanks in liquid-liquid operations due to regions of flow stagnation. As well, Hemrajani and Tatterson (2004) as well as Leng and Calabrese (2004) observed that solids, in solid-liquid mixing, typically accumulated in the bottom corners of flat bottom tanks where the turbulence and circulation was low (also known as dead zones). Generally, flat bottom tanks contain areas of low fluid

velocity, which are not optimal for liquid-liquid or liquid-solid mixing. As such, higher impeller speeds are required to compensate for flat-bottomed tanks (Mak, 1992).

Dished heads (ASME dished, elliptical, or torispherical) are optimal for inducing the flow patterns required for solid suspension (Atiemo-Obeng et al., 2004). Liquid-liquid dispersion experiments are typically performed in a flat bottom tank however, the reasons for this are unclear. One possible reason may be the difficulty in producing a dished head made of glass, as is typically used in liquid-liquid dispersions for use of a Laser Doppler Anemometer (LDA).

2.4.2 Impellers

Impellers can be separated into two general classes: axial flow and radial flow impellers. Axial flow impellers are characterized as primarily downward pumping with a majority of their energy dissipation translated into pumping of the fluid (i.e. they have a high pumping efficiency but a low shearing capability). The flow pattern generated by axial impellers can be seen in **Figure 2.2**. As illustrated, a single circulation loop is formed, which is ideal for blending and solids-suspension. Radial flow impellers typically dissipate a majority of their energy via shearing of the liquid (i.e. high shear and low pumping efficiency). **Figure 2.3** illustrates the two circulation loops (one below and one above the impeller) that are formed as the fluid is pushed radially from the impeller region. Leng and Calabrese (2004) recommend that axial impellers (e.g. hydrofoils and propellers), should have a D/T ratio between 0.4 and 0.6 while radial disk turbines should have a D/T ratio between 0.25 and 0.4. Both types of impellers are commonly used in liquid-liquid dispersions (Hemrajani and Tatterson, 2004).

The Lightnin® A-310 hydrofoil is a commonly used axial flow impeller. It was designed to have a low shear rate but a very high pumping rate. Two literature power numbers can be seen in **Table 2.2**.

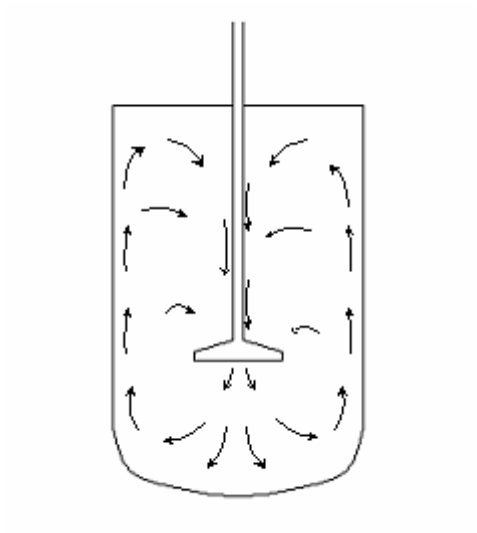

Figure 2.2: Flow Patterns Created by Axial Impellers

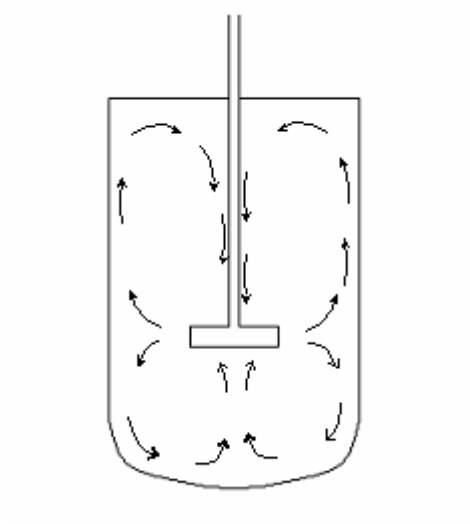

Figure 2.3: Flow Patterns Created by a Rushton Turbine

Table 2.2 Literature Power Numbers for Hydrofoil

Np	Source
0.3	Hemrajani & Tatterson, 2004
0.4	Lightnin LABS

The Lightnin® R-100 Rushton Turbine, RT, is a commonly used radial impeller and has a very high shear rate. It primarily moves the liquid in the radial direction; however, depending on impeller clearance, it can produce some axial flow (Hemrajani & Tatterson, 2004). **Table 2.3** contains RT power numbers from various sources.

Table 2.3 Literature Power Numbers for Rushton Turbine

Np	Source
5.2	Weetman, 2004
5.5	Laity and Treybal (1957)
5.75	Lightnin LABS
6.2	Rushton et al. (1950)

The power numbers, Np, stated in **Tables 2.2** and **Table 2.3** are from experiments using various tank geometries with the Lightnin® A-310 hydrofoil or the Rushton Turbine, respectively. As mentioned earlier, tank geometry has a significant effect on Np; therefore, all the power numbers are not considered to be comparable. Instead, they indicate a range of common values associated to each of these two impellers.

2.4.3 Liquid Height

The liquid height, H, in liquid-liquid mixing influences the homogeneity of the tank contents. The minimum and maximum liquid height for adequate suspension is usually specified with respect to the tank diameter. Using a single impeller, optimal flow patterns in liquid-liquid mixing occur between an H/T ratio of 1.0 to 1.2 (Leng and Calabrese, 2004). Additionally, Atiemo-Obeng et al.

(2004) recommend an H/T ratio of less than 1.3 in solid-liquid mixing (for a single impeller). If the H/T ratio is larger in liquid-liquid or liquid-solid mixing, two impellers should be used to achieve uniform suspension and homogeneity. Most liquid-liquid mixing research to date (Chen and Middleman, 1967; Arai et al., 1977; Okamoto et al., 1981; Calabrese et al., 1986; Zhou and Kresta, 1998; Pacek et al., 1999; Baldyga et al., 2001) has been performed in circular, flat-bottomed tanks with an H/T ratio of 1.

2.4.4 Impeller Clearance

The height of the impeller above the bottom of the tank is commonly referred to as the clearance, C. Similar to the liquid height, the clearance is usually expressed as a ratio of the tank diameter. The clearance of the impeller can also have a very large impact on the energy dissipation rate within the system. A wide variety of clearances have been used in the literature. Experiments by Arai et al. (1977), Calabrese et al. (1986), and Pacek et al. (1999) used a C/T of 0.5, while Baldyga et al. (2001) used 0.25. In research performed by Chen and Middleman (1967), an impeller clearance of one impeller diameter was used.

Holmes et al. (1964) examined the optimal clearance of a Rushton Turbine by determining the circulation times of the two flow loops within the vessel (see **Figure 2.3**). The circulation time is defined as the average residence time of a particle as it exits the impeller region, proceeds around the loop and returns to the impeller region. As can been seen, a top circulation loop and a bottom circulation loop are created when using a Rushton Turbine. Mixing between the two circulation loops occurs primarily in the impeller region. By adjusting the clearance of the impeller, the circulation times, t_c, of each loop is altered. The circulation times of each loop are approximated using:

$$t_c = \frac{\omega}{n}\left(\frac{T}{D}\right)^2 \qquad (2\text{-}28)$$

where the value of ω, 0.85, is an empirical constant (Holmes et al., 1964).

For a radial impeller placed in the vertical center of a tank, the circulation time of each loop is nearly the same. In this case, if a pulse of an immiscible liquid was injected into the impeller region, the bulk of the pulse in the top circulation loop would return to the impeller region at the same time as the bulk of the pulse in the bottom loop. Because the bulk portions of immiscible liquid from each circulation loop return to the impeller region at the same time, only the bulk portions are mixing and the mixing time required to reach a homogenous dispersion will be very long. However, at an alternate impeller clearance the circulation times of each loop will be different and the pulse would return from each loop at different times. Therefore, the bulk of the immiscible liquid pulse in the bottom circulation loop returns to the impeller region and mixes with the liquid from the top circulation loop which has no immiscible liquid. At this impeller clearance, the time required to create a homogenous dispersion will be much shorter due to the mixing of liquid with a high concentration of immiscible liquid with liquid with only a small concentration of immiscible liquid.

2.5 Literature Review Conclusion

Chapter 2 has provided a basis for the experimental setup of the current study. Using this chapter as a guideline, the mixing tank and assembly can be built to resemble those found in literature. **Chapter 3** describes the experimental setup and compares the current apparatus with those found in the literature review. By developing a mixing tank similar to that found in literature, experiments which have been performed by other authors can be reproduced and compared thereby calibrating the equipment. **Chapter 4** begins with these calibration experiments. Once the equipment has been validated, **Chapter 4** investigates the previously unknown relationship between highly viscous (bitumen) droplets and the energy dissipation rate.

List of References

Arai K., Konno M., Matunaga Y., Saito S. (1977) Effect of Dispersed-Phase Viscosity on the Maximum Stable Drop Size for Breakup in Turbulent Flow. *Journal of Chemical Engineering of Japan*, v.10, 325-330.

Atiemo-Obeng V.A., Penney W.R., Armenante P. (2004) Chapter 10: Solid-Liquid Mixing, in *Handbook of Industrial Mixing; Science and Practice*, E.L. Paul, V.A. Atiemo-Obeng, S.M. Kresta, eds., Wiley-Interscience, New Jersey, 543-584.

Baldyga J., Bourne J.R., Pacek A.W., Amanullah A., Nienow A.W. (2001) Effects of Agitation and scale-up on drop size in turbulent dispersions: allowance for intermittency. *Chemical Engineering Science*, v.56, 3377-3385.

Batchelor, G.K., (1953) The Theory of Homogenous Turbulence. Cambridge, UK, Cambridge Univ. Press. (*Cambridge Phil. Soc. Proc.* **47**, 359.)

Berkman, P.D., and Calabrese, R.V., (1988) Dispersion of viscous liquids by turbulent flow in a static mixer. *AIChE J.* **34**, 602-609.

Bertrand, J., Couderc, J.P., Angelino, H., 1980, Power consumption, pumping capacity and turbulence intensity in baffled stirred tanks: comparison between several turbines. *Chem. Eng. Sci.* **35**, 2157-2163.

Brodkey, R.S., 1975, *Turbulence in Mixing Operations*, Academic Press, New York.

Brown D.E., and Pitt, K,. (1974) Drop size distribution of stirred non-coalescing liquid-liquid system. *Chem. Eng. Sci.* **27**, 577-583.

Calabrese R.V., Chang T.P.K., Dang P.T. (1986) Drop Breakup in Turbulent Stirred-Tank Contactors Part I: Effect of Dispersed-Phase Viscosity. *AIChE J.*, v.32, no. 4, 657-666.

Chen H.T., Middleman S. (1967) Drop Size Distribution in Agitated Liquid-Liquid Systems. *AIChE J.*, v.15, no. 5, 989-995.

Coulaloglou, C.A., and Tavlarides, L.L., (1976) Drop size distribution and coalescence frequencies of liquid-liquid dispersions in flow vessels. *AIChE J.* **22,** 289-297**.**

Dyster, K.N., Koustakos, E., Jaworski, Z. and Nienow, A.W., 1993, An LDA study of the radial discharge velocities generated by a Rushton turbine: Newtonian fluids, Re≥5. *Trans IChemE*, **71**, Part A, 11-23.

Hemrajani R.R., Tatterson G.B. (2004) Chapter 6: Mechanically Stirred Vessels, in *Handbook of Industrial Mixing; Science and Practice*, E.L. Paul, V.A. Atiemo-Obeng, S.M. Kresta, eds., Wiley-Interscience, New Jersey, 345-391.

Hinze, J.O., (1955) Fundamentals of the Hydrodynamic Mechanism of Splitting in Dispersion Processes. *AIChE J.* **1**, 289-295.

Holmes, D.B., Voncken, R.M., Dekker, J.A. (1964) Fluid flow in turbine-stirred, baffled tanks-I, Circulation time. *Chem. Eng. Sci.*, **19**, 201-208.

Kolmogoroff, A.N. (1941a). The local structure of turbulence in incompressible viscous fluids for very large Reynolds numbers, *Compt. Rend. Acad. Sci. USSR*, 30, 301-305.

Kolmogoroff, A.N. (1941b). Dissipation of energy is locally isotropic turbulence, *Compt. Rend. Acad. Sci. USSR*, 32, 16-18.

Kolmogoroff, A.N. (1949) The Breakup of Droplets in a Turbulent Stream. *Dok. Akad. Nauk.*, **66**, 825.

Laufhutte, H.D. and Mersmann, A., 1985, Laser-Doppler velocimetry as a suitable measuring technique for determination of flow behavior in stirred fluids. *Ger. Chem. Eng.* **8**, 371-379.

Leng D.E., Calabrese R.V. (2004) Chapter 12: Immiscible Liquid-Liquid Systems, in *Handbook of Industrial Mixing; Science and Practice*, E.L. Paul, V.A. Atiemo-Obeng, S.M. Kresta, eds., Wiley-Interscience, New Jersey, 639-753.

Mak A.T.C. (1992) Solid-liquid mixing in a Mechanically Agitated Vessel, Ph.D. dissertation, University-College-London.

Marshall E.M., Bakker A. (2004) Chapter 5: Computational Fluid Mixing, in *Handbook of Industrial Mixing; Science and Practice*, E.L. Paul, V.A. Atiemo-Obeng, S.M. Kresta, eds., Wiley-Interscience, New Jersey, 257-343.

Nienow A.W. (2004) Break-up, Coalescence and Catastrophic Phase Inversion in Turbulent Contactors. *Advances in Colloid and Interface Science*, v.108-109, 95-103.

Nishikawa, M., Mori, F., and Fujieda, S., (1987) Average drop size in a liquid-liquid phase mixing vessel. *J. Chem. Eng. Japan* **20**, 454-459.

Okamoto Y., Nishikawa M., Hashimoto K. (1981) Energy Dissipation Rate Distribution in Mixing Vessels and its Effects on Liquid-Liquid Dispersion

and Solid-Liquid Mass Transfer. *International Chemical Engineering*, v.21, no.1, 88-94.

Pacek A.W., Man C.C., Nienow A.W. (1998) On the Sauter Mean Diameter and Size Distributions in Turbulent Liquid/Liquid Dispersions in a Stirred Vessel. *Chemical Engineering Science*, vol.53, no.11, 2005-2011.

Pacek A.W., Chamsart S., Nienow A.W., Bakker B. (1999) The Influence of Impeller Type on Mean Drop Size and Drop Size Distribution in an Agitated Vessel. *Chemical Engineering Science*, v.54, 4211-4222.

Ranade, V.V. and Joshi, J.B., 1989, Flow generated by pitched blade turbines I: measurements using laser Doppler anemometer. *Chem. Eng. Commun.* **81**, 197-224.

Ranade, V.V. and Joshi, J.B., 1989, Flow generated by pitched blade turbines II: Simulation using K – ε model. *Chem. Eng. Commun.* **81**, 225-248.

Rushton, J.H., Costich, E.W., Everett, H.J., (1950a) Power characteristics of mixing impellers-Part I. *Chem. Eng. Prog.* **46,** 395-404.

Rushton, J.H., Costich, E.W., Everett, H.J., (1950b) Power characteristics of mixing impellers-Part II. *Chem. Eng. Prog.* **46,** 467-476.

Weetman R.D.J. (2004) Chapter 22: Role of the Mixing Equipment Supplier, in *Handbook of Industrial Mixing; Science and Practice*, E.L. Paul, V.A. Atiemo-Obeng, S.M. Kresta, eds., Wiley-Interscience, New Jersey, 639-753.

Zhou G., Kresta S.M. (1998) Correlations of Mean Drop Size and Minimum Drop Size with the Turbulence Energy Dissipation and the Flow in an Agitated Tank. *Chemical Engineering Science*, v.53, no.11, 2063-2079.

Chapter 3
Experimental Design

3.1 Introduction

The geometric characteristics of a mixing tank are important factors influencing the flow patterns required to create liquid-liquid dispersions. Solid-liquid mixing was not performed in this study; however, the experimental apparatus was designed such that this could be achieved in future studies. This chapter describes the experimental equipment and procedures used in this study. Discussion will also be given on the calibration of the experimental equipment and analytical instruments. Finally, determination of the experimental fluids used to develop the relationship between ε_{max} and d_{max} will be discussed.

3.2 Experimental Setup

The objective of the experimental apparatus is to measure the droplet size as the energy dissipation rate, ε, is changed. The experimental setup is illustrated in **Figure 3.1**. The device can be described as four separate components: the mixing tank, lid, motor/mixer, and data collection/analysis instrumentation.

3.2.1 The Mixing Tank

As stated in **Chapter 2**, most liquid-liquid dispersions use flat bottom tanks; however, Leng and Calabrese (2004) recommend dished heads for both liquid dispersions and solid-liquid dispersions. Dished heads enable the flow patterns required for liquid-liquid operations (Leng and Calabrese, 2004). A dished head was selected because it contains less stagnant zones than flat bottom tanks. The mixing tank was constructed using an 8” schedule 40 ASME Dished Head and a 386 mm length of 8”, schedule 40 pipe was used as the tank wall. To prevent corrosion of the mixing tank, the entire interior was painted with marine paint.

To prevent solid body rotation in the tank, four equally spaced wall baffles were installed (Hemrajani and Tatterson (2004)). The baffles were 184 mm long

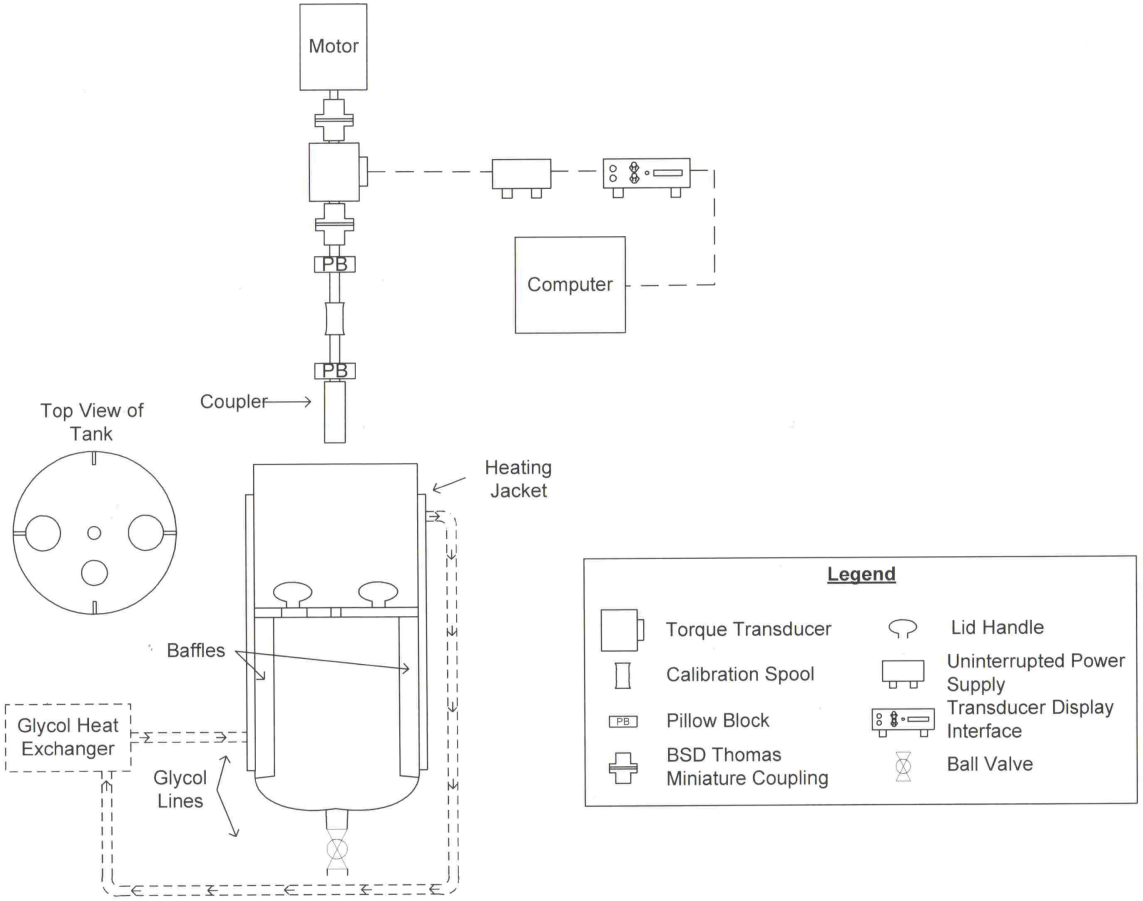

Figure 3.1: Schematic Diagram of Mixing Tank Assembly

and were placed such that the bottoms of the baffles extended to the start of the ASME dished head. The baffles were 20 mm wide (~T/10 as per Hemrajani and Tatterson) and welded such that a 6 mm gap existed between the baffle edge and the tank wall. This gap prevented dead zones from existing along the length of the baffle.

A ¾” pipe was inserted flush with the bottom of the tank to drain the contents. A NCS ¾” ball valve was fitted on the pipe to control drainage. The pipe has a volume of 0.0445 L open to the tank during operation. Due to this space being confined from the remainder of the tank, this volume of liquid may stay relatively quiescent as compared to the remainder of the tank. Due to the extremely small volume of this pipe as compared to the rest of the tank (~ 0.7 % of tank volume) it was assumed that it did not affect the mixing within the tank. The working (8” pipe) portion of the tank (i.e. not the ASME head) is jacketed such that the temperature of the tank contents can be controlled. This is achieved by pumping heated or cooled glycol through the jacket using a glycol heater/pump.

3.2.2 Mixing Tank Lid

A lid was designed to prevent aeration of the bitumen within the tank. Aeration occurs when bitumen is being mixed in the tank and consequently attaches (preferentially) to the water / air interface. To minimize surface energies, bitumen tends to spread spontaneously at the air / water interface, resulting in a thin layer of oil which separates the air and water phases. Without a lid to prevent aeration, bitumen that reaches the water / air interface stays at the free surface and is no longer part of the dispersion. To prevent bitumen adhering to the lid, the lid was made of typical soda lime glass. The soda glass is hydrophilic and repels the bitumen, thereby facilitating the bitumen remaining in suspension.

A 14.3 mm hole was placed in the center of the lid for the impeller shaft and a 31.75 mm hole, with an accompanying plug, was created to allow for bitumen addition to the system. The lid rests on the top of the baffles. The small gap between the lid and tank wall is sealed while in use by applying a silica gel.

During operation of the tank, an H/T ratio of 1.16 was chosen such that optimal solid-liquid and liquid-liquid flow patterns would prevail (as discussed in **Section 2.4.3**). Water is filled to a point above the top of the lid in order to eliminate all air space (i.e. prevent aeration) and ensure the desired flow patterns will prevail within the tank. Zhou and Kresta (1998) showed that submersion of the lid had no effect on the mean drop size or flow patterns within the tank.

3.2.3 Motor/Mixer Device

The motor selected for the mixing operation is a ½ horsepower Pacific Scientific 90 volt motor capable of 3450 rpm. The motor is located directly above the center of the tank and spins a 3/8" shaft. The torque is measured using an E300/RWT Raleigh Wave Rotary Torque Transducer from Sensor Technology Limited. BSD Thomas Miniature Couplings were located on each side of the transducer to protect it from vibration. The shaft alignment is fixed using two press-fit, self-aligning ball bearings in separate supports. A 20 mm diameter spool was placed between the supports to allow for the suspension of a known weight for calibration of the transducer. Beneath the bottom support, a shaft coupler is fitted to the drive shaft to allow for the connection of the shaft and impeller.

Two impellers were used in this study: a hydrofoil and a Rushton turbine. Specifications for each impeller can be found in **Table 3.1**. Additionally, photographs of the impellers can be viewed in **Figure 3.2A/B**. Each impeller has a different bore diameter; therefore two different shafts were fabricated and tapered to fit the shaft coupler. The shafts had a common length of 438 mm. The shaft designed for the hydrofoil was tapered, from 3/8" to 7/16", just above the impeller, while the Rushton turbine shaft was tapered, from 5/16" to 7/16", 230 mm from the bottom.

Figure 3.2A: Photo of the Hydrofoil

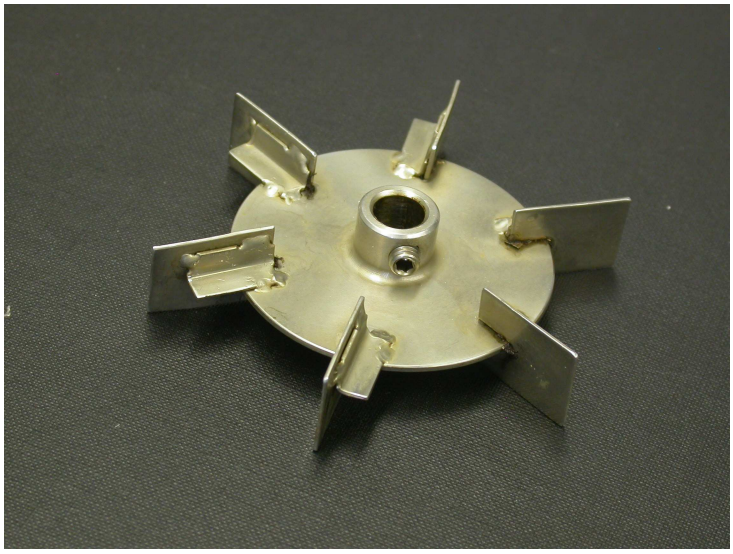

Figure 3.2B: Photo of the Rushton Turbine

Table 3.1: Impeller Specifications

Type	Diameter	Bore Diameter	Material	Pitch	Design
Hydrofoil	3.4"	3/8"	316 SS	-	Lightnin® A-310
Rushton Turbine	3"	5/16"	316 SS	-	Lightnin® R-100

3.2.4 Data Collection/Analysis Instrumentation

Sensor Technology Ltd. produced the display software for the transducer. In the setup, the transducer measures the torque and sends the signal to the E302 Advanced Rayleigh Wave Torque Transducer Display Interface Module. The interface module is connected to a computer via a serial cable and the TorqSense software outputs the rotation speed and torque in real time. The software is also capable of logging the data.

A three wire Resistance Temperature Detector (RTD), factory calibrated between 0°C and 200°C is used to measure the fluid temperature within the tank. The RTD was inserted through the tank bottom and protrudes 15 mm into the fluid. It is assumed that no temperature gradients exist within the fluid during mixing. The thermocouple data is converted to a 4-20 mA signal using a temperature transmitter and subsequently displayed using Delogger software.

A Sony DSP 3CCD color video camera was used to film the tank internals. A frame rate of 1/500 second was required to prevent the bitumen droplets from appearing as streaks in the frames. Further discussion regarding camera setup and usage is detailed in **Section 3.3.4**.

3.3 Equipment Calibration

The experimental apparatus required a variety of calibration experiments to ensure its results were in agreement with other liquid-liquid dispersion experiments. Calibration of the transducer, software, and camera are all described in this section.

3.3.1 Torque Transducer Calibration

The first piece of equipment that required calibration was the torque transducer. The experimental error of the torque transducer is 0.005 N·m (±0.25 % of full scale deflection) while the error in the angular velocity was 0.3 rpm (±0.1% at minimum experimental speed). To check the accuracy of this equipment, the following experiment was performed.

The motor/mixer assembly was tilted and laid horizontally on a lab bench with the 20 mm diameter spool hanging over the edge. The flexible couplings were removed to prevent deflection of the shaft. A bucket of sand with a weight (F) of 51.84 N was hung from the spindle using a 0.4 mm diameter fish line. The moment arm, b, of the fish line and spool apparatus was 10.2 mm. The bucket was attached to the end of the line, and the motor power was adjusted such that the bucket was suspended at a constant height above the ground. Finally, the applied torque was calculated using the relation:

$$M = Tq = F \cdot b \tag{3-4}$$

The value of M thus obtained is then compared to the torque reported by the transducer/software. The transducer display output oscillated between 0.525 and 0.530 N·m and the calculated required torque was 0.529 N·m. Repeated experiments produced the same result and it was concluded that the transducer was measuring and reporting the torque within the manufacturer's specified error of 0.005 N·m.

3.3.2 Power Number Calibration

Ideally, the maximum energy dissipation rate for this study should be measured for comparison with literature values. However, the use of a Laser Doppler Anemometer (LDA) is required to perform this measurement. Application of an LDA was impossible due to the steel construction of the tank. An acrylic tank could not procured within the required time of this study. Instead,

the average energy dissipation rate was used as a preliminary comparison for the mixing tank apparatus.

In these experiments, de-ionized (DI) water was mixed using a hydrofoil and a Rushton turbine. The results from the experiments can be seen in **Figures 3.3** and **3.4**. As the Reynolds number, Re, increases to 10^6, the scatter of the data decreases; this is consistent with the change from the transitional to a fully turbulent regime. Therefore, to alleviate variance in the results, only experiments with a Reynolds number above 10^6 will be used in the power number calculation.

The hydrofoil had average power numbers of 0.303 and 0.314 in experiments 1 and 2, resulting in a difference of 0.011. The error in this calculation (Holman, 1978) was calculated to be 0.006 at 2000 RPM based on manufacturer's errors of 0.005 N·m error in the torque and 0.3 rpm error in the rotational speed while an error of 0.1 mm was used for the diameter of the hydrofoil. The calculated error of 0.006 allows two values to be within 0.012 of each other (0.006 each) and is shown to be greater than the experimental error of 0.011. In addition, both numbers lie within the power number range specified in literature to be between 0.3 and 0.4 (**Table 2.2**).

For the Rushton turbine, average power numbers of 3.73, 3.76, and 3.78 were obtained. The error in these values is 0.03 and was calculated using the same errors in the hydrofoil experiment. Again, the error bars of these values all overlap and the power numbers are proven to be consistent. However, the power numbers obtained here are significantly less than those reported by other authors as seen in **Table 2.3**. A majority of the power numbers reported in the table used flat-bottomed tanks, whereas the current setup has a dished head. As discussed in **Section 2.4.1**, dished heads are primarily used in applications where good circulation within the tank is required (i.e. solid suspension). Therefore, using a dished head creates more circulation within the tank which may account for the lower than expected power numbers (see **Section 4.3.2.1** for discussion of power law constant effect on results).

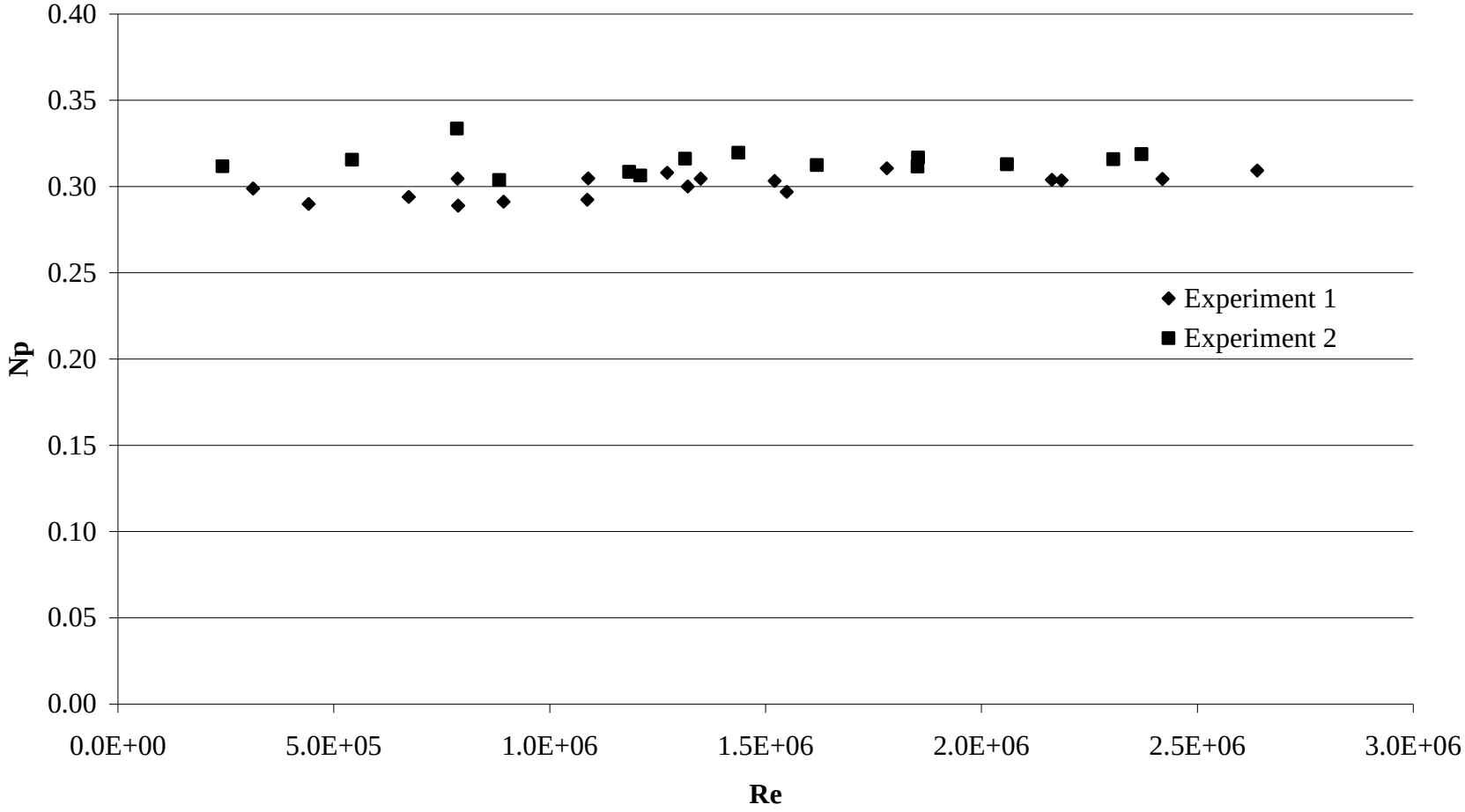

Figure 3.3 Power Number of the Hydrofoil

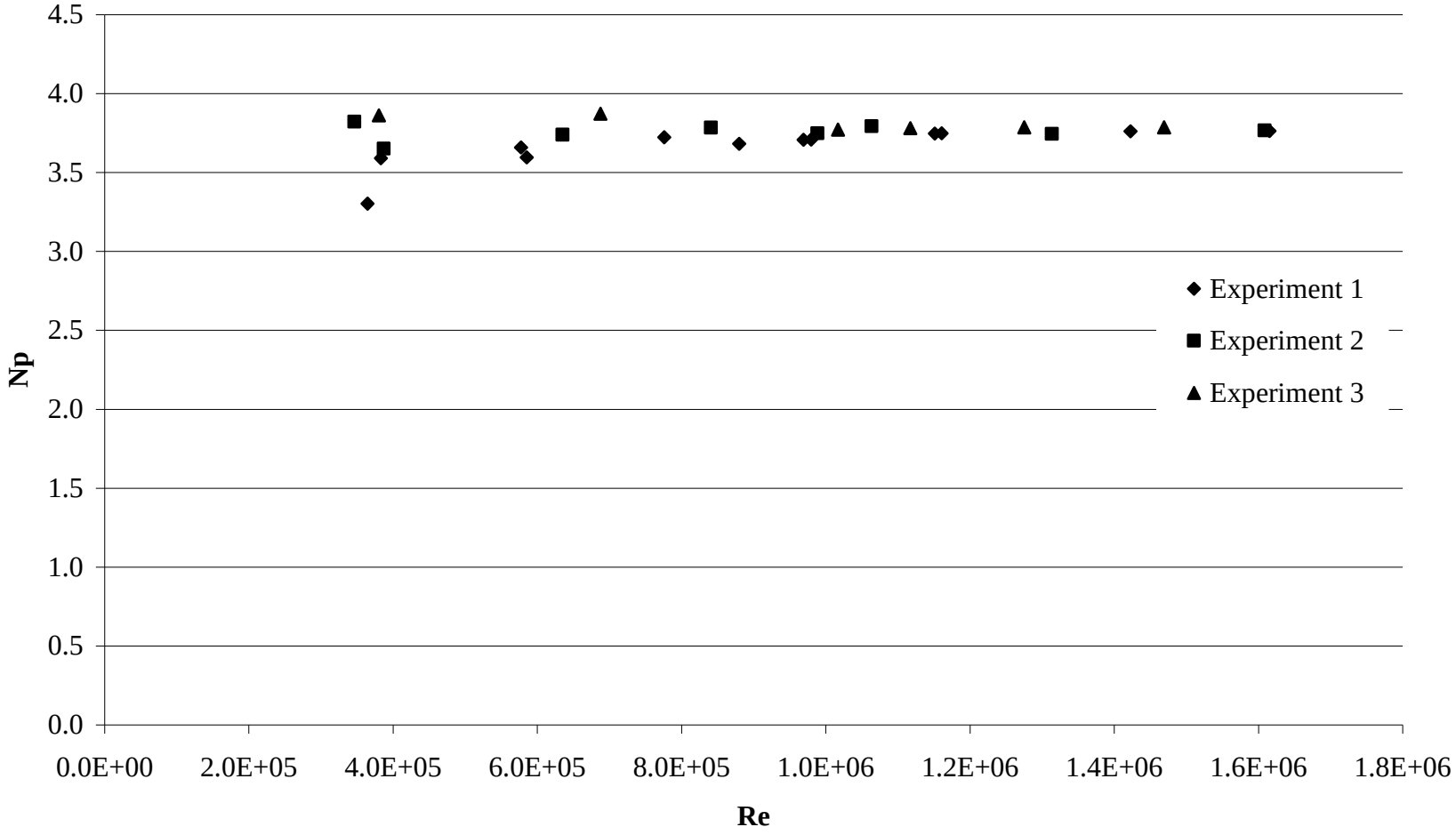

Figure 3.4 Power Number of the Rushton Turbine

3.3.3 Minimum Calculable Droplet Size

During experimentation, a Sony DSP 3CCD color video camera was used to film the liquids within the tank. The video is subsequently converted to a series of bitmaps and DaVis 6 software is used to analyze the bitmap sequences. Each bitmap image is 640 by 480 pixels in size. The software identifies droplets within the image based on gradients of light intensity. To determine the accuracy of the software, an analysis of known droplet sizes was performed. On a 640 pixel by 480 pixel image, a series of circles, ranging in size from 3 pixels to 100 pixels, were drawn (**Figure 3.5**) and subsequently analyzed using the software (**Figure 3.6**). As can be seen in **Figure 3.6** the light colored circle outlines on each dark circle are the approximation by DaVis for the size of the circle (i.e. in the experiment, the droplet size). As illustrated in **Figure 3.7**, the percent error between the actual circle size and the DaVis estimated size increases substantially for circle diameters less than 20 pixels. Therefore, the minimum droplet size that can be confidently reported within 2% error is 20 pixels (actual size of 0.82mm, see **Section 3.3.5**). Although mean diameters (e.g. d_{32}, d[v,10], d[v,50], or d[v,90]) cannot be calculated without being able to confidently calculate the smaller droplet sizes, the maximum droplet size, d_{max}, can be reliably reported by the software provided it is larger than 20 mm Therefore, the maximum droplet size will be the focus of this study.

3.3.4 Software Calibration

Prior to calibration of the camera, the adjustable parameters of DaVis 6 were specified such that the largest droplets within a series of bitmaps were depicted accurately. The largest droplets were chosen for software calibration because d_{max} is the focus of this study. As illustrated in **Figure 3.8**, changing the adjustable parameter known as the “Global Threshold” affects the number of droplets and, to a smaller extent, their reported sizes. Therefore, a Global Threshold, based on visual inspection of the bitmaps, was set to 10% due to its ability to closely outline the largest bitumen droplets. The remaining three

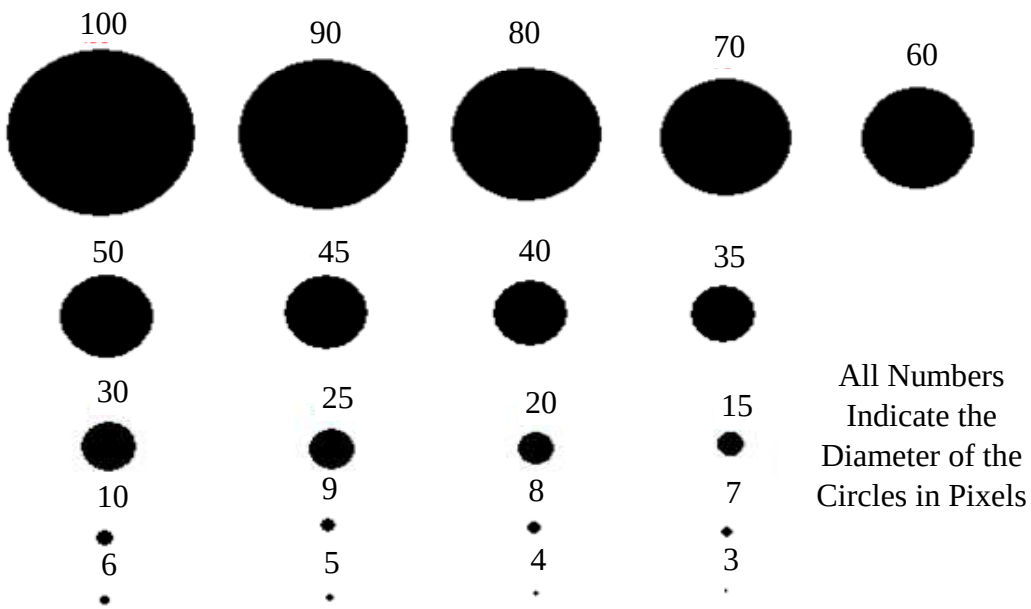

Figure 3.5 Circles Created in Paint for Software Analysis

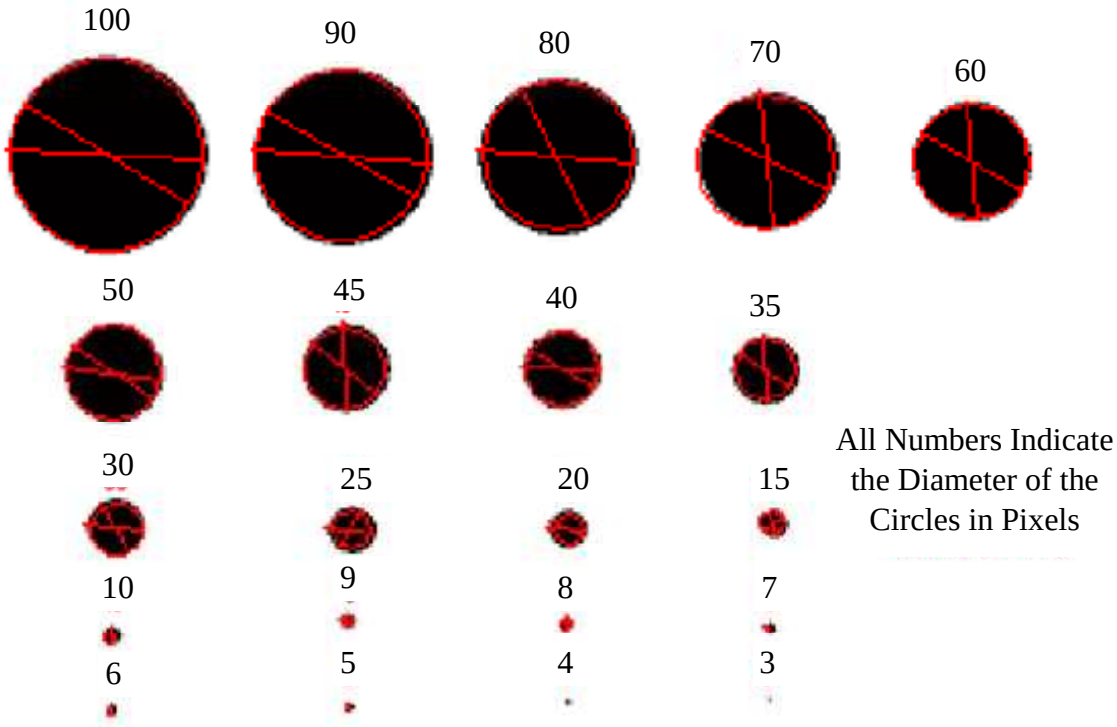

Figure 3.6 DaVis Analyzed Circles

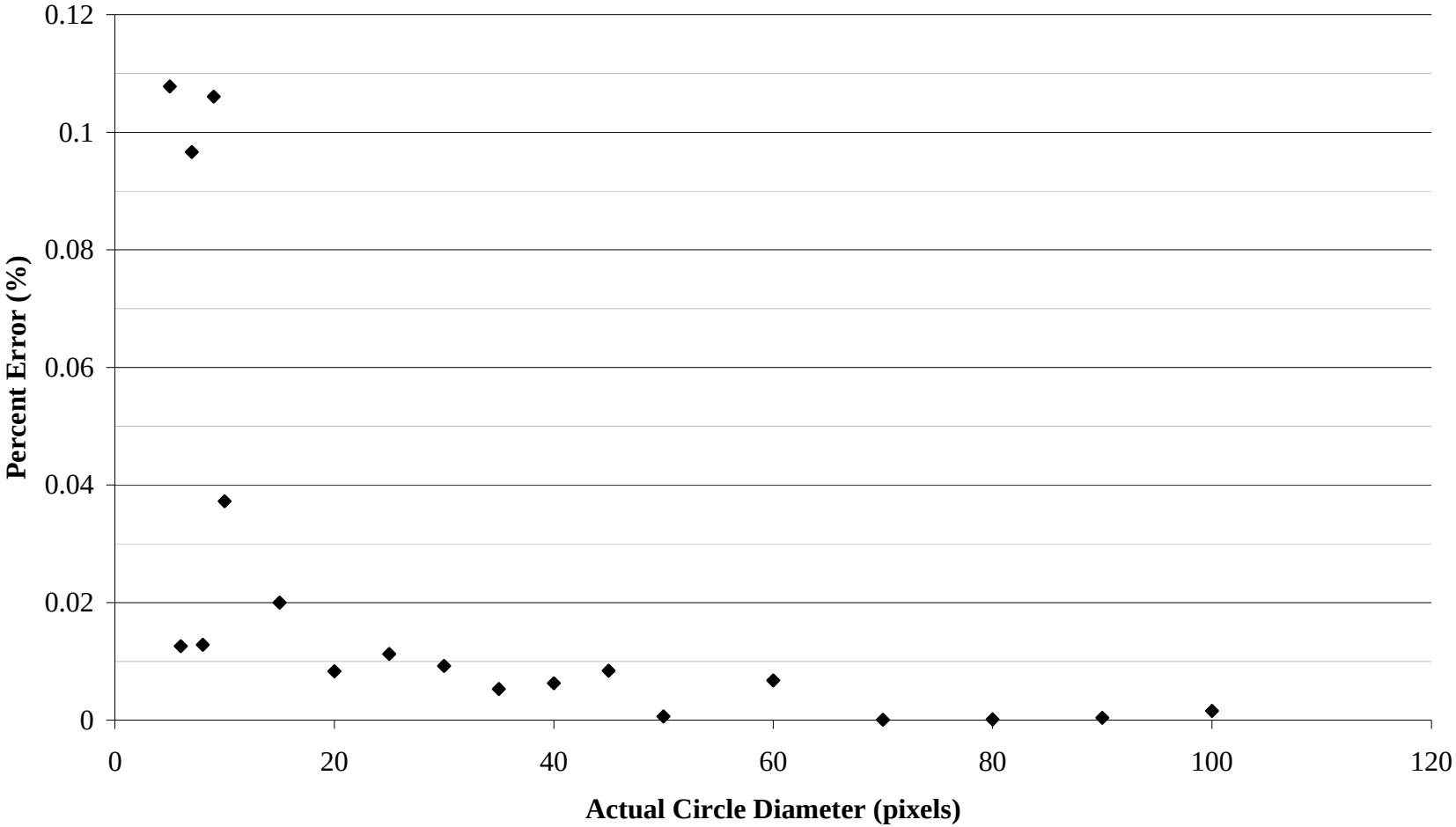

Figure 3.7 Percent Error between Actual Circle Diameter and DaVis Circle Diameter

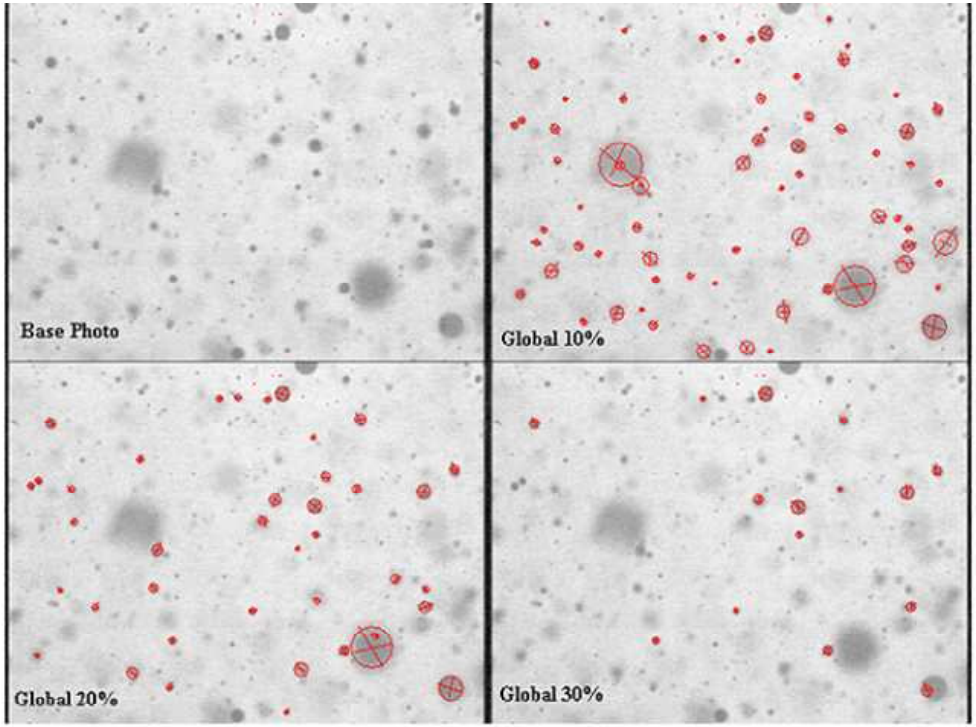

Figure 3.8 Global Composites

adjustable parameters, Minimum Threshold, High Level, and Low Level all had no effect on d_{max}.

3.3.5 Camera Calibration

In order to determine the focal position, camera position, and frame height required for the most accurate results, an experiment using 0.5 mm glass beads (soda lime) from BioSpec Products Inc. instead of an immiscible liquid was performed. The purpose of using the standardized glass beads was to video an experiment where the droplet sizes (i.e. the bead sizes) were precisely known. Coanda Research and Development Corp. (Vancouver) analyzed a sample of the glass beads using a Malvern Mastersizer S long bed Ver. 2.19; the results are shown in **Table 3.2**. The results did not include the maximum droplet size. d[v,90] was the closest value to d_{max} reported and therefore this statistic was used to calibrate the camera settings using the glass beads.

Table 3.2: Coanda Results for Glass Beads

Mean Diameters	d(v,10)	d(v,50)	d(v,90)	d32
Size (um)	455.12	522.41	583.28	517.92

The focal point of the camera was slightly inside the interior of the viewing window. This focal length was chosen to ensure that no bitumen droplets were magnified in size due to their presence between the viewing window and the focal point. **Figure 3.9** shows a variety of mean droplet diameters types found via visual inspection of the bitmaps. Visual inspection and measurement were required because the glass beads were too transparent for the DaVis 6 software to detect. As can be seen, the largest frame height gives a d[v,90] most similar to the results from Coanda (0.583 mm). It was deduced that, as the frame height increases, the accuracy of d[v,90] improves. To obtain the largest frame height, the camera was placed in a variety of positions away from the tank. In all these experiments, the camera's aperture was fully opened and the focal point was adjusted to remain slightly inside the viewing window.

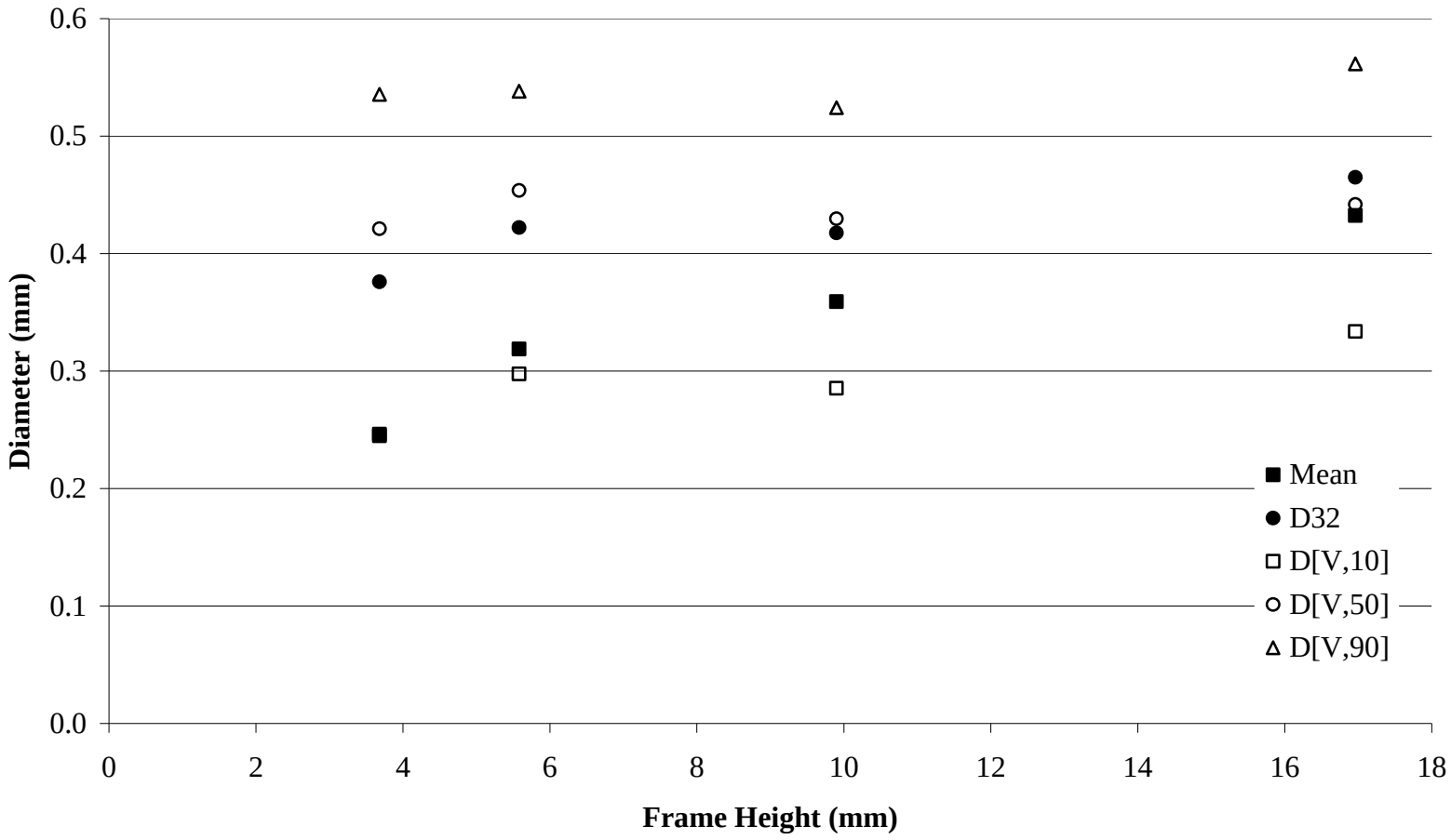

Figure 3.9 Droplet Distribution vs Frame Height

Figure 3.10 illustrates the frame height as a function of the camera distance from the tank. To determine the camera distance required to obtain the maximum frame height, the derivative of the quadratic equation in **Figure 3.10** was taken and set to zero. The resultant maximum frame height achievable is 19.7 mm and can be seen by locating the camera at a distance of 261 mm from the tank. Therefore, for an actual height of 19.7 mm (or a bitmap height of 480 pixels) each pixel is 0.041 mm in height (and length since it is square). Based on this pixel height, the minimum calculable droplet size of 20 pixels (as seen in **Section 3.3.3**) translates to an actual minimum calculable droplet size of 0.821 mm using this camera setup.

Figure 3.11 compares two experimental results (using the camera parameters obtained above) to Coanda's. The experimental errors for d[v,10] and d[v,50] are larger than that of d[v,90] due to beads identified beyond the focal point. Consequently, the beads are sized smaller than their actual size, thereby decreasing the size of the reported d[v,10] and d[v,50] in this study. The error between this study and Coanda for d[v,90] is fairly negligible:1.6% and 4.4% error for experiments 1 and 2 respectively.

3.4 Experimental Fluids

Careful selection of the continuous and dispersed fluids was required to ensure a dispersion of bitumen within the aqueous system. The following section describes the selection process for the two fluids.

3.4.1 Bitumen Selection

At different stages during oil sands extraction and upgrading, bitumen has much different characteristics. The bitumens have different densities and viscosities and contain differing quantities of fines, clays, water, sulfur, heavy metals, etc. In addition, bitumen originating from different mines will also have slightly different properties and impurities. Atmospheric Topped Bitumen (ATB) from Syncrude Canada Ltd. was used in this study.

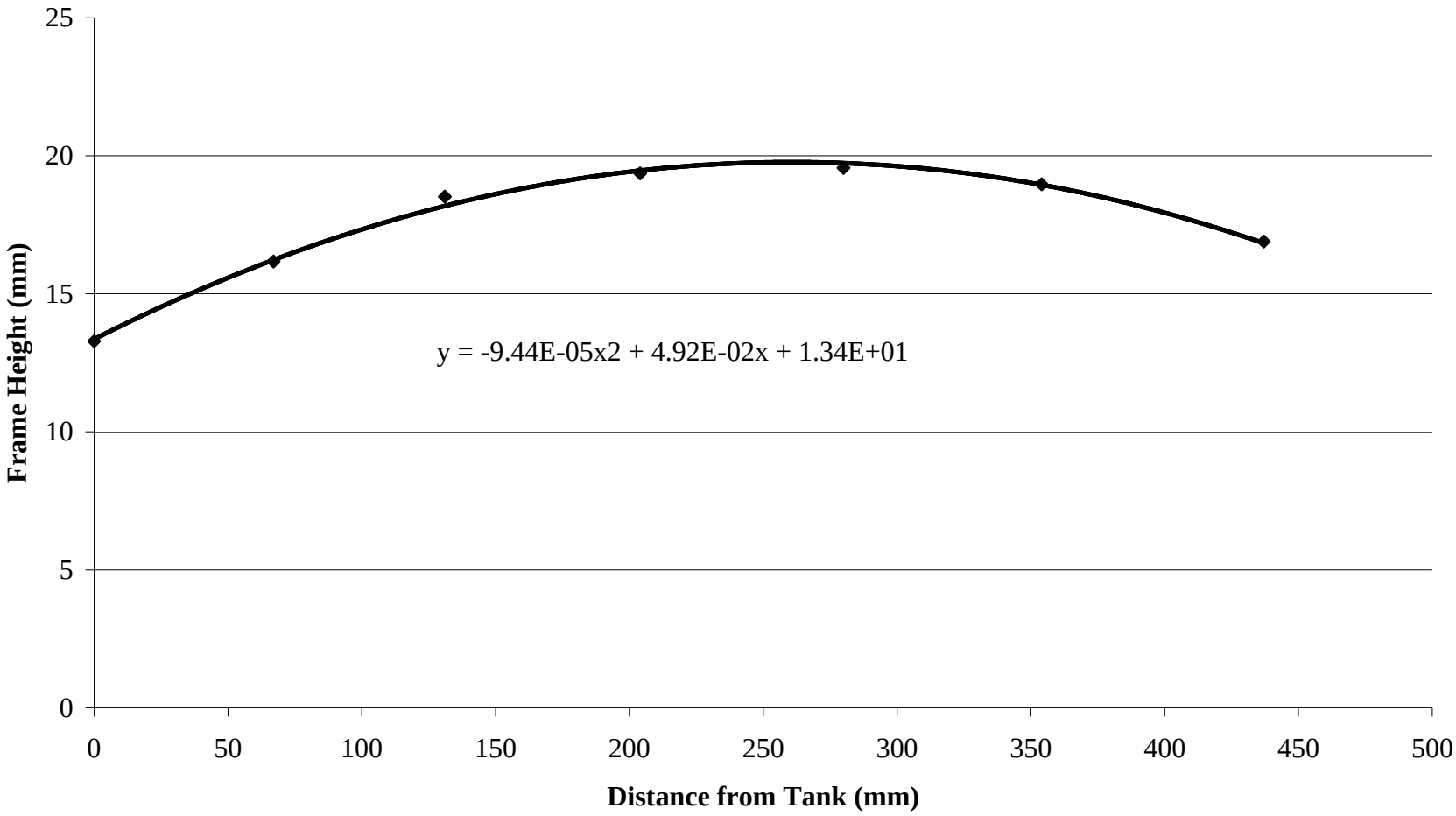

Figure 3.10 Frame Height as a function of Camera Distance from Tank

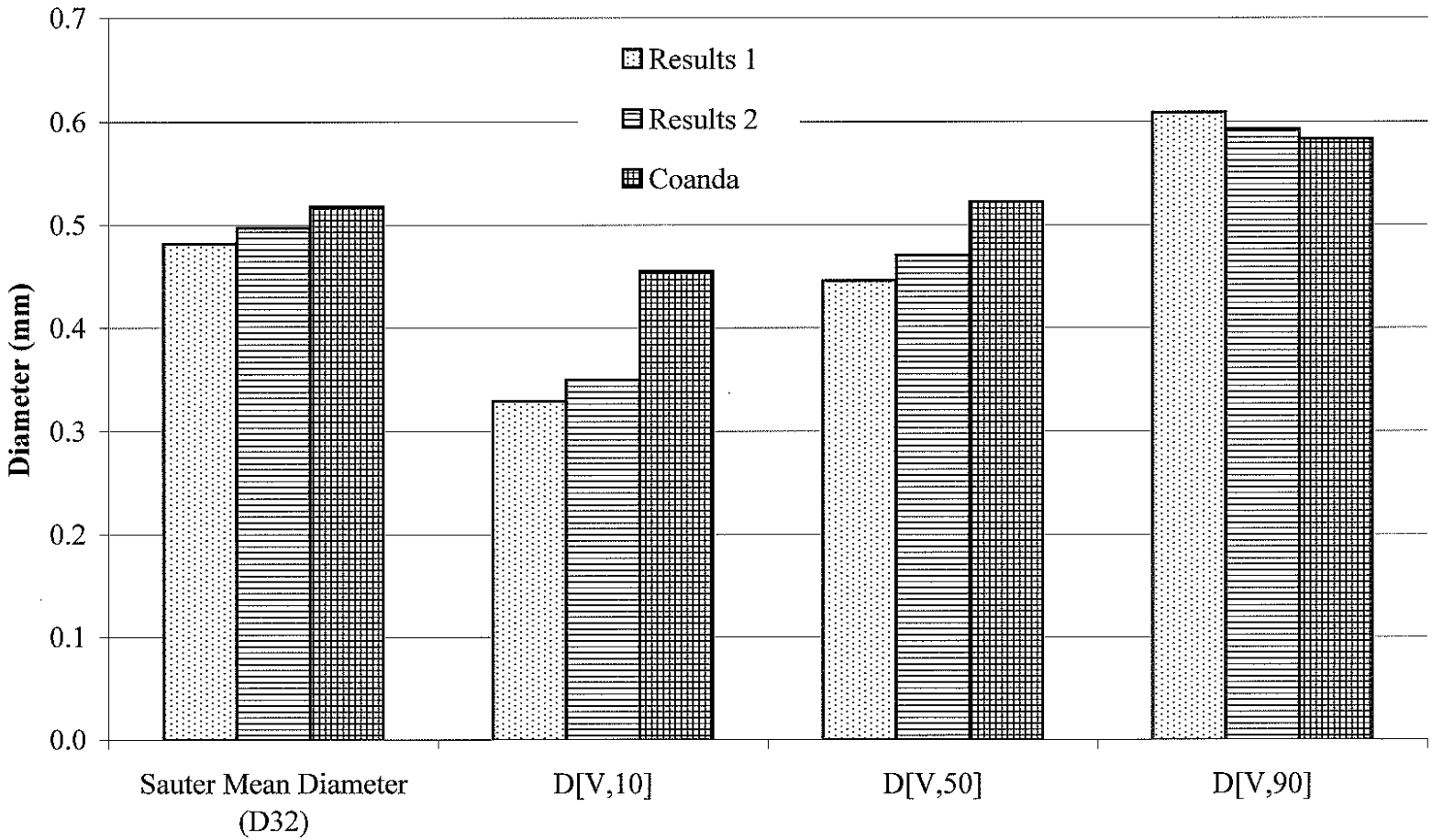

Figure 3.11 Comparison Between Current Study Analysis and Coanda

ATB originates from an early stage in the upgrading process. After bitumen is separated from the sand and collected as a froth from the Primary Separation Vessel, it is diluted with naphtha. Subsequently, the diluted bitumen undergoes centrifugation or inclined plate settling to remove water and solids. The diluted bitumen is then sent to the Diluent Recovery Units (DRU). The DRUs operate at atmospheric pressure and are responsible for three functions:

1) *Naphtha Recovery* – The DRUs distill off the naphtha in order to reuse the expensive diluent
2) *Light Gas Oil Recovery* – Light Gas Oil is fractionated and sent directly to the light gas oil hydrotreater
3) *Hot ATB Production* – Hot ATB is produced for feed to the LC-Finer hydroprocessor and Vacuum Distillation Unit (VDU)

The hot ATB produced in this process has undergone water and solids removal and only the lightest hydrocarbon fraction has been removed. Therefore, the density and viscosity of ATB are similar to that of bitumen in the hydrotransport process. In addition, the viscous forces in equation (2-25) are much greater than the interfacial tension forces by satisfying the following equation:

$$\tau_s << \tau_d \qquad \text{and} \qquad C_5 \left(\frac{\rho_c}{\rho_d} \right)^{1/2} \frac{\mu_d \left(\varepsilon_{\max} d_{\max} \right)^{1/3}}{\sigma} \approx 300 >> 1$$

where C_5 was calculated by Hinze (1955) to be approximately 0.725.

Based on these arguments, ATB was selected as the best candidate for this study.

Figure 3.12 illustrates the exponential-like relationship between temperature and viscosity for ATB. As illustrated, the trend line of ATB closely resembles the CO_2 bitumen of Svrcek and Mehrotra (1982). The difference in viscosity may be attributed to the type of bitumen used and the ore quality from which the bitumen was extracted. It is important to note that, at the experimental temperature of 50ºC, the viscosity of the ATB is 21.5 Pa·s. At this temperature, a

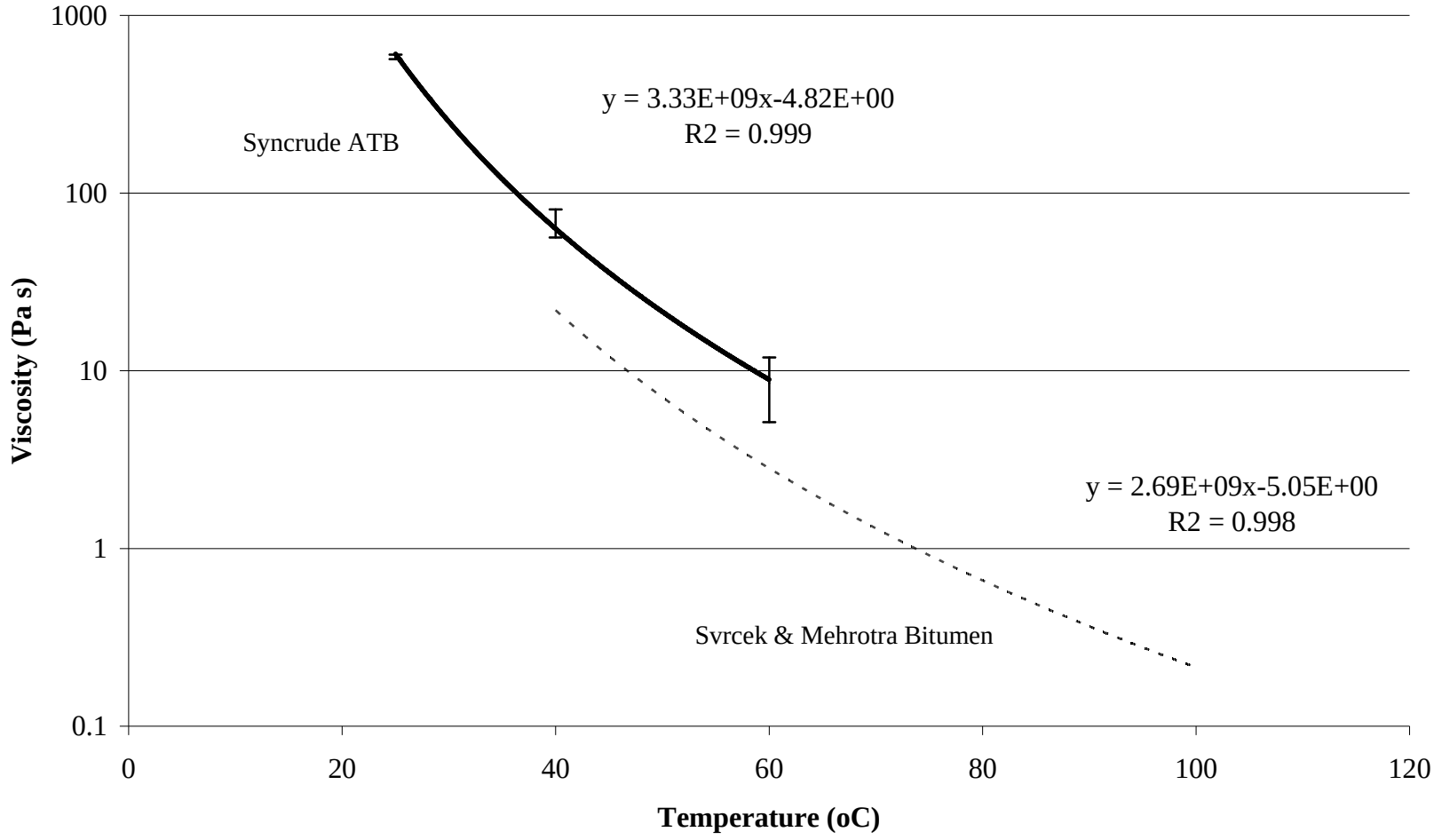

Figure 3.12 Bitumen Viscosity as a function of Temperature

variation of 1ºC affects the viscosity by ~ 10%. **Table 3.3** illustrates the compositions of ATB used in this experiment.

Table 3.3 Atmospheric Topped Bitumen (ATB) Characteristics

Characteristics	Units	Temp	Overall Mean	Median
Density	(kg/m3)	25°C	1020	1019
		30°C	1016	1016
Ash	(wt%)		0.82	0.83
C_6 - Asphaltenes	(wt%)		16.7	17.2
Dynamic Viscosity	(cP)	25°C	583649	582722
		40°C	68569	62000
		60°C	8522	6920
Kinematic Viscosity	(cSt)	40°C	59214	60095
Conradson Carbon Residue	(wt%)		14	14.5
Micro Carbon Residue	(wt%)		14.8	15
Carbon	(wt%)		82.6	82.6
Hydrogen	(wt%)		10.2	10.2
Nitrogen	(wt%)		0.5	0.5
Oxygen	(wt%)		1.1	1
Sulphur	(wt%)		5.1	5.3
Nickel	(mg/kg)		76	80
Vanadium	(mg/kg)		205	212
Iron	(mg/kg)		573	654
Simulated Distillation				
IBP	(°C)		242	245
25% off	(°C)		422	440

3.4.2 Continuous Phase (Water) Selection

It was important to select a continuous phase composition that prevented bitumen-glass adhesion and bitumen-bitumen coalescence. Bitumen adhesion to the viewing window would have prevented video recording of the tank internals while adhesion to the window and/or lid would have caused a diminishing concentration of suspended bitumen. Three types of water were tested: Tap water with salts (NaCl, $NaHCO_3$, and Na_2SO_4), DI water with no salts, and Simulated Process Water (SPW). The composition of tap water can be seen in **Table 3.4**.

SPW is made using de-ionized (DI) water and adding three salts: 25 mM of NaCl, 15 mM of $NaHCO_3$, and 4 mM of Na_2SO_4.

Table 3.4: Tap Water Quality Analysis

Water Quality	Units	7-day Average
Hardness	(mg/L $CaCO_3$)	182.2
pH		7.71
Temperature	(^oC)	17.8
Chlorine Residual	(mg/L)	2.031
Alkalinity	(mg/L)	126.5
Conductivity	(µS/cm)	433.8
Caustic Soda Dose	(mg/L)	23.12

3.4.2.1 Water Selection: Theoretical Considerations

As discussed previously, no bitumen coalescence is desired during the experiment. Tap water contains significant quantities of impurities such as calcium, magnesium, bicarbonates, and sulphates. Moran (2004) showed that the probability of coalescence with the addition of 10 ppm Ca^{2+} to a NaCl solution, increased from 45% to 78%. Therefore, bitumen coalescence increased substantially with the addition of a trace amount of calcium. Additionally, recent studies by Basu et al. (2004) have shown than an increase in the calcium dosage (as $CaCl_2$ or $CaSO_4$) for a water/bitumen system results in a less negative bitumen zeta potential, thereby causing a higher probability of coalescence. This may be due to calcium adsorption at the bitumen interface (decreased surface charge) or to an increased ionic concentration in the solution (double layer compression). These conclusions were a result of observations of a decreasing static contact angle between glass and bitumen with additional calcium. Based on these observations, all efforts to minimize Ca^{2+} concentrations within the tank should be exercised. Therefore, tap water, with 165 mg/L of $CaCO_3$ would likely increase adhesion and coalescence within the system.

DI water is devoid of any Ca^{2+} and other polyvalent cations. Although this water will not cause additional glass-bitumen adhesion or bitumen coalescence, it does nothing to prevent it. Ions may leach out of the bitumen within the system and cause bitumen-glass adhesion or bitumen coalescence.

Analyzing the surface charges in the system, an attraction exists between positively charged glass and negatively charged bitumen. The sodium ions introduced by SPW prevent this ionic attraction. As can be seen in **Figure 3.13**, the sodium ions are attracted to the negative surface of the bitumen and form an electric double layer around the bitumen particles, thereby creating an electrostatic repulsion between the bitumen droplets and the glass. The SPW also contains CO_3^{2-} from the dissociation of $NaHCO_3$. The CO_3^{2-} is important because, in the presence of Ca^{2+} ions, a precipitate of $CaCO_3$ is formed, thereby removing Ca^{2+} from the system. Therefore, the small amount of $NaHCO_3$ included in the SPW acts as a safeguard to remove any trace Ca^{2+} within the system. From the above discussion, it was expected that the SPW would be the best aqueous solution for this experimental study.

3.4.2.2 Water Selection: Experimental Considerations

To empirically determine the water chemistry most effective in preventing bitumen coalescence and glass adhesion, a bench scale experiment was devised. Three glass beakers were each filled with 1.5 L of one of the three types of water discussed above and heated to 50°C on a ThermaMix 201 hotplate/stirrer. The components were agitated using a Teflon-coated magnetic stirrer. The rotational speed of the stirrer was kept low enough such that no air was entrained. ATB was added in 0.2g increments to a total weight of 0.8g (~ 0.05 %wt). The extent of bitumen dispersion and glass adhesion was observed and recorded.

In the experiment using tap water with salts, a large amount of bitumen quickly adhered to both the glass and plastic impeller while only a very small portion remained dispersed in the water. In both runs with DI water, a good dispersion was created with very minimal amounts (1 or 2 drops) attaching to the

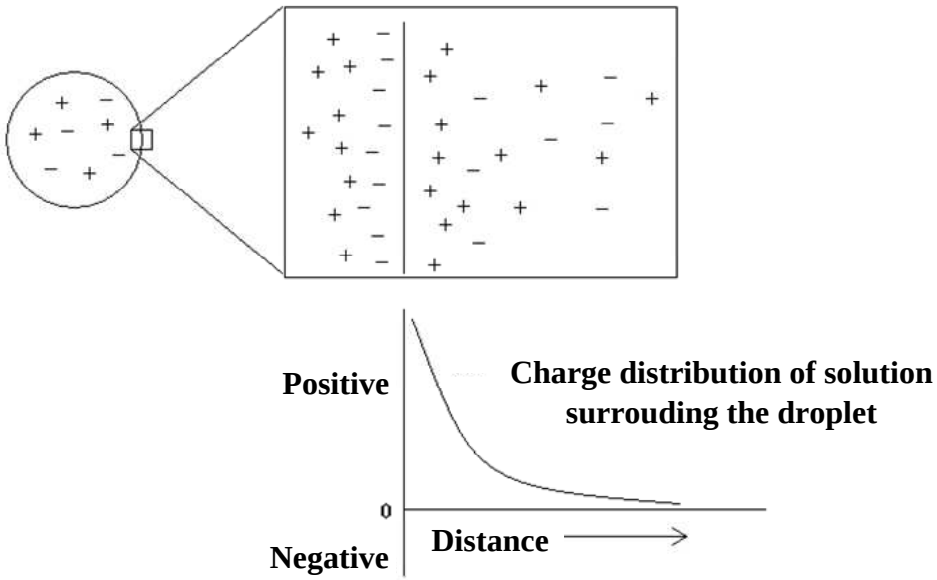

Figure 3.13 Electrical Double Layer Around Bitumen

glass. Since the DI water had no salts, suspended bitumen droplets readily coalesced with droplets attached to the wall. In SPW, the very small quantity of droplets attached to the beaker wall did not increase in size. Thus, it was deemed that DI water, with 25 mM NaCl, 15 mM $NaHCO_3$, and 4 mM $NaSO_4$ (i.e. SPW), was the best option for the experiment.

3.5 Experimental Operations

Chapter 2, and the above portion of **Chapter 3** were used to develop the experimental and analytical procedures for this study. An outline of the procedure for determining the effects of energy dissipation rate on the bitumen droplet size can be found in the following section.

3.5.1 Experimental Procedure

- Make 8 L of Simulated Process Water (SPW) by adding 11.69 g of NaCl, 10.08g of $NaHCO_3$, and 2.27g of Na_2SO_4 to 8 L of DI water
- Heat 2L of SPW to 70ºC using a hot plate and set the glycol temperature for the tank heating jacket to 55ºC
- Add heated SPW to tank and heat additional 4L of SPW to 60ºC
- Add 4L of heated SPW and 0.7L of room temperature SPW to tank
- Place glass lid into mixing tank and rest on baffles. Drain any SPW that is above the lid (should be minimal)
- Use Superflex Clear RTV silicone adhesive sealant to seal the space between glass lid and tank wall. Allow 30 minutes to dry
- Heat the remaining SPW to xºC as calculated below (found via an energy balance between the water in the tank and the remaining water to be added):

$$x = 237.6 - 3.94y \qquad (3\text{-}1)$$

where y is the temperature of the water in tank and x is the temperature of the water to be added.

- Position and turn on both 500 W photography lights and turn impeller to 100 RPM to keep SPW circulating within tank
- Allow water temperature to reach equilibrium and adjust heating jacket temperature if required to maintain a water temperature within the tank of 50°C
- Once a constant SPW temperature is achieved, remove the lid plug and add 1.7 g of bitumen using a long spoon. To add the bitumen, place the spoon near the impeller and shake softly such that bitumen detaches from spoon
- Once a majority of the bitumen has detached from spoon, remove the spoon and replace the lid plug immediately

SPW was used in this experiment as per the findings in **Section 3.4.2**. A water temperature of 50ºC was selected for this experiment. This temperature was chosen such that the bitumen viscosity was lower than at room temperature, thereby increasing the ease of handling. In addition, the temperature of 50ºC is similar to operating temperatures of existing industrial oil sands conditioning process.

A dispersed phase volume fraction, Φ, of ~0.00025 was used for the bitumen experiments. It is significantly lower than those specified by other authors (see **Table 2.1**) to ensure that no coalescence occurred during mixing. This precaution was taken because no dispersions with bitumen-like viscosities have been investigated - and the intent of this preliminary study was to investigate dispersion in the absence of droplet coalescence. Furthermore, a much lower concentration was used due to the unknown effects of impurities inherent in Atmospheric Topped Bitumen (ATB) which may cause enhanced coalescence efficiency.

3.5.2 Analysis Procedure

During the experiment, video was taken using the high speed camera setup outlined in **Section 3.3.5**. The video was started immediately prior to the addition

of bitumen. Analysis of the video was achieved using Adobe Photoshop, DaVis 6 Software, and Microsoft Excel. The following data analysis sequence was used in this study:

- Use Adobe 6 to record 20 second intervals of video onto the computer. For example, the first time interval would begin 1 minute after initial bitumen addition and proceed to 1 minute and 20 seconds after initial bitumen addition
- Repeat 20 second time interval recording starting at 2, 4, 8, 12, 20, 30, 40, 60 , 80, 100, and 120 minutes after initial bitumen addition
- Convert each clip to a bitmap sequence using Adobe Photoshop. At 500 frames per second, 10 000 frames will be available per time interval recording. For each interval, convert every 100th frame of film to a bitmap to create a bitmap sequence 100 frames long
- Transfer all sequences to DaVis 6 software and convert .bmp files to .imx format using a picture of the back tank wall as the reference for the light intensity within the tank
- Analyze each series of .imx's using the following Davis 6 variables (as determined in **Section 3.3.4**):
    - Global Threshold: 10
    - Minimum Threshold: 36
    - Hi Level: 30
    - Low Level: 25
- Export resulting text file (.txt) into excel (.xls) and determine the maximum droplet size

The value of d_{max} reported for each experiment was an average of several time intervals. Typically, the first four interval times (i.e. d_{max} resulting from the first 8 minutes) were not used due to the large bitumen droplet size variance within the tank. There were large gradients within the tank because not all bitumen droplets had been exposed to the impeller region in the tank. The

remaining values of d_{max} were averaged, resulting in the reported d_{max} for the experiment.

Calculation of ε_{max} was done using equation (2-14):

$$\varepsilon = C_3 N^3 D^2 \tag{2-14}$$

Zhou et al. (1998) calculated the value of C_3 for several different tank geometries as discussed in **Section 2.2.4**. The current study's geometry resembles a setup used by Zhou et al., as seen in **Table 3.5**. They performed five experiments using this geometry to find the C_3 required for calculation of ε_{max}. For the hydrofoil, the average C_3 value from the five experiments was 0.967 while the Rushton turbine value was 12.14. Therefore, the following equations will be used for calculating the ε_{max} in each system:

$$\varepsilon_{max} = 0.967 N^3 D^2 \quad \text{Hydrofoil} \tag{3-2}$$

$$\varepsilon_{max} = 12.14 N^3 D^2 \quad \text{Rushton Turbine} \tag{3-3}$$

Table 3.5: Geometry Comparison

Parameter	Current Study	Zhou (1997)
Baffles	4	4
Impeller Diameter, D	0.375T	0.475T
Clearance, C	0.375T	0.333T
Average Re (*10^{-4})	3.9	12.21
Bottom of Tank	Dished	x

The error of ε_{max} was found using the uncertainly analysis as outlined by Holman (1978). Standard manufacturer's errors of 0.3 rpm for the rotational rate and 1 mm for the impeller diameter were used to calculate the error. The error for the Hydrofoil was found to be 2.3% while the error for the Rushton Turbine was found to be 2.6%. These values will be used in Chapter 4 when calibrating the

experiment and when determining the maximum droplet size - maximum energy dissipation rate relationship.

Although the current study's experimental apparatus is not an exact replica of that used by Zhou (1998), the C_3 value determined in Zhou's experiment is the closest representation available. In the current study, this value will provide only the magnitude of ε_{max} and will not have any effect on the power law exponent. Therefore, although the value of C_3 is an estimate based on an experimental setup slightly different from what is used in the current study, only the magnitude of ε_{max} will be affected - not the trend or power law exponent. Since the power law exponent, and therefore the relationship between the droplet size and the energy dissipation rate, will not be affected, the third objective outlined in **Section 1.4** can still be achieved without additional error being introduced.

3.6 Conclusions

The experimental setup was designed similarly to other liquid-liquid mixing apparatuses; the major difference here was the selection of a dished bottom instead of a flat bottom tank. It is believed that due to this deviation and the resulting improvement in circulation, the Rushton turbine power numbers obtained in this study were lower than literature values.

Equations (3-2) and (3-3) will be used for calculating the maximum energy dissipation rate ε_{max} in the tank. Due to restrictions in identifying droplets less than 0.82 mm in diameter, the effects of ε_{max} on d_{max} will be investigated rather than a different mean diameter (see **Section 2.2.1** for other mean diameters).

Atmospheric Topped Bitumen (ATB) was selected for this study due to its similarity in density and viscosity to bitumen in the hydrotransport process. In addition, ATB has relatively low concentrations of impurities. Simulated Process Water (SPW) was chosen as the continuous fluid for its ability to limit bitumen adhesion to the glass viewing window and to aid in the prevention of bitumen droplet coalescence.

List of References

Atiemo-Obeng V.A., Penney W.R., Armenante P. (2004) Chapter 10: Solid-Liquid Mixing, in *Handbook of Industrial Mixing; Science and Practice*, E.L. Paul, V.A. Atiemo-Obeng, S.M. Kresta, eds., Wiley-Interscience, New Jersey, 543-584.

Basu S., Nandakumar K., Lawerence S., Masliyah J. (2004) Effect of Calcium Ion and Montmorillonite Clay on Bitumen Displacement by Water on a Glass Surface. *Fuel*, v.83, issue 1, 17-22.

Hemrajani R.R., Tatterson G.B. (2004) Chapter 6: Mechanically Stirred Vessels, in *Handbook of Industrial Mixing; Science and Practice*, E.L. Paul, V.A. Atiemo-Obeng, S.M. Kresta, eds., Wiley-Interscience, New Jersey, 345-391.

Holman J.P. (1978) Experimental Methods for Engineers, Magraw Hill, 3rd edition.

Leng D.E., Calabrese R.V. (2004) Chapter 12: Immiscible Liquid-Liquid Systems, in *Handbook of Industrial Mixing; Science and Practice*, E.L. Paul, V.A. Atiemo-Obeng, S.M. Kresta, eds., Wiley-Interscience, New Jersey, 639-753.

Moran, K. (2004) Coalescence of Small Bitumen Droplets, *5th International Conference on Petroleum Phase Behavior and Fouling*, Banff, Alberta, June 13-17, 2004, paper #75.

Svrcek, W.Y., Mehrotra, A.K. (1982) Gas Solubility , Viscosity, and Density Measurements for Athabasca Bitumen. *J. Can. Petroleum Tech.*, **Jul-Aug**, 31-38.

Zhou G. (1997) Characteristics of Turbulence Energy Dissipation and Liquid-Liquid Dispersions in An Agitated Tank, Ph.D. dissertation, University of Alberta.

Zhou G., Kresta S.M. (1998) Evolution of Drop Size Distribution in Liquid-Liquid Dispersions for Various Impellers. *Chem. Eng. Sci.*, v.53, no.11, 2099-2113.

Chapter 4
Results and Discussion

4.1 Introduction

In **Chapter 2**, the design specifications for a liquid-liquid dispersion were investigated and in **Chapter 3** the specific design and calibration of the current experimental setup were discussed. This chapter will begin with verification of the experimental apparatus by investigating low viscosity oils, similar to that used in the studies discussed in **Chapter 2**. Next, a water-bitumen study will be performed and compared to literature results and theory (**Section 2.3.4**). The focus of this chapter will be on the effect of ε_{max} on d_{max}.

4.2 Model Oils

A comparison between this study and literature results was first made to validate the experimental setup and procedure. By using a fluid with a viscosity similar to those used in the studies investigated in **Chapter 2** (viscosity is ~1-2 Pa·s; herein called the "model oil"), a direct comparison can be made. This section will illustrate the model oil guidelines and selection criteria.

4.2.1 Model Oil Selection

Selection of the model oil for comparison with other studies depended largely on two factors:

1) The ability for the DaVis software to capture oil droplet profiles as bitmap images, and
2) the ability to suspend the model oil in water for an extended duration of mixing

In order for the software to detect the oil droplets, the droplets had to be sufficiently opaque such that the software could distinguish them from the continuous medium. Additionally, in order for the droplets to be quantified by the software, the droplet size must be sufficiently large such that their sizes could be analyzed accurately (see **Section 3.3.3** for acceptable droplet sizes). It is also

important that the dispersed droplet density was near that of water such that the dispersed phase remained suspended within the continuous medium and did not accumulate at the top of the tank.

After investigating motor oils, gear oils, and viscosity standards, the model oil was chosen to be a toluene/bitumen mixture based on the aforementioned requirements. To determine the toluene-bitumen (T/B) ratio required to create a mixture with a viscosity of ~ 2 Pa·s at 25°C, the viscosities of a 0.122 T/B mixture and a 0.249 T/B volume ratio were determined using a Brookfield Programmable DV-II Viscometer. A temperature of 25°C was used such that existing toluene and bitumen viscosity data could be used. Based on linear interpolation (see **Figure 4.1**) between these two points, a 2 Pa·s mixture could be created using a T/B ratio of ~0.15. As illustrated on **Figure 4.1**, a T/B ratio of 0.15 gave a viscosity of 2.66 Pa·s. In addition, with a low percentage of toluene in the mixture, the density was nearly that of bitumen; thus satisfying the requirement that the model oil density was near that of water.

The same experimental procedure described in **Section 3.5.1** was used except that the toluene-diluted-bitumen was added using a wide-mouthed syringe instead of a spoon due to the significantly lower viscosity of the model oil. For the model oil experiments, a Rushton turbine was used.

4.2.2 Model Oil Results

The trend between d_{max} and ε_{max} for the model oil system can be seen in **Figure 4.2**. A power law relationship with an exponent of -0.25 was produced from eight experiments with varying energy dissipation rates. Within the eight runs, one experiment was repeated at a similar dissipation rate to test the reproducibility. The percent difference between the two points is 1.04% thereby indicating that the experiment is reproducible. This power law exponent was then plotted on **Figure 4.3** with data acquired by Arai (1977) for a variety of dispersed phase viscosities. Extrapolating Arai's data, a power law exponent of -0.237 was expected. In comparison with the current study's value of -0.251, the power law exponent is within experimental error of Arai's data.

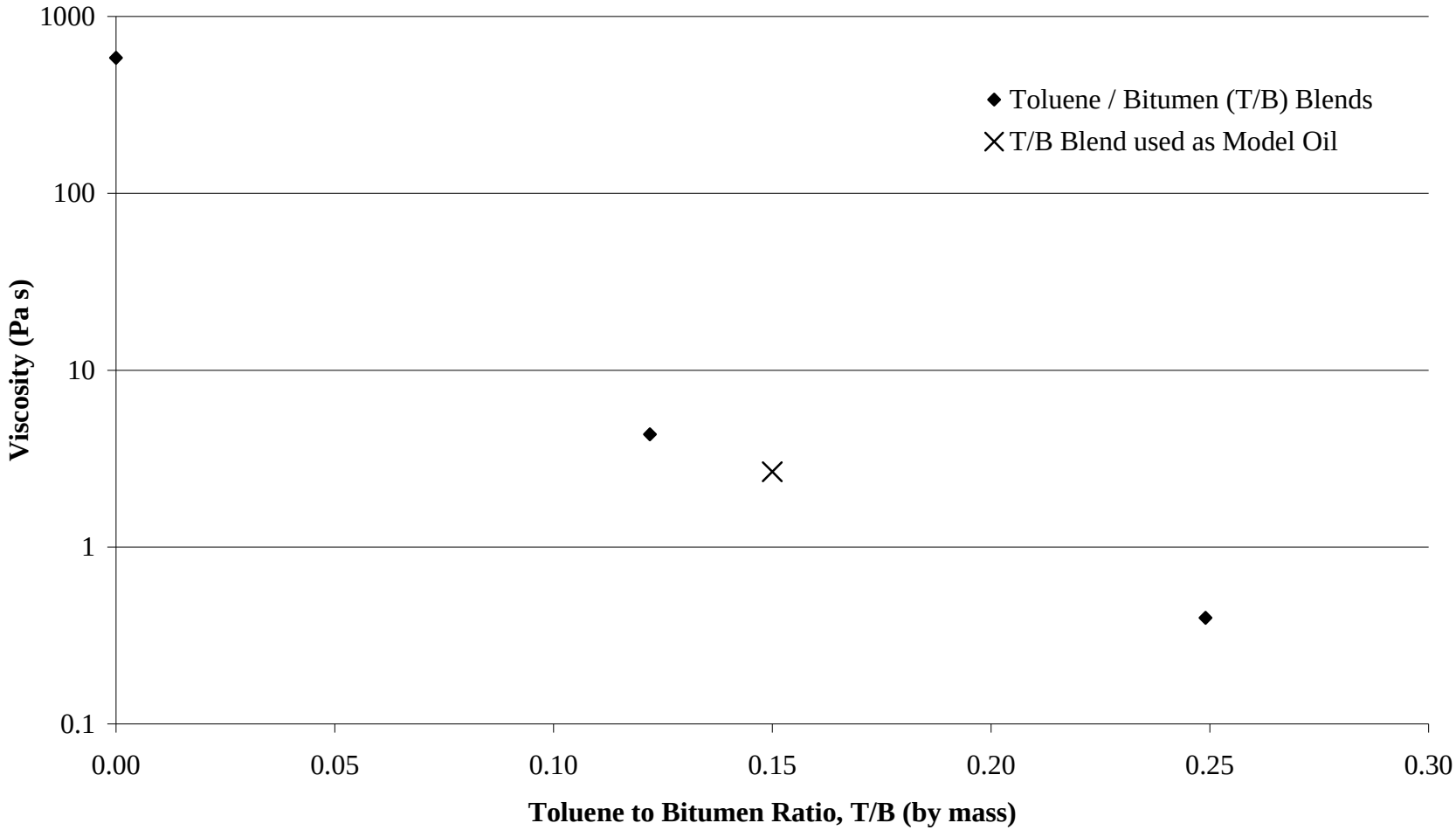

Figure 4.1: Viscosity vs Toluene/Bitumen Ratio at 25°C

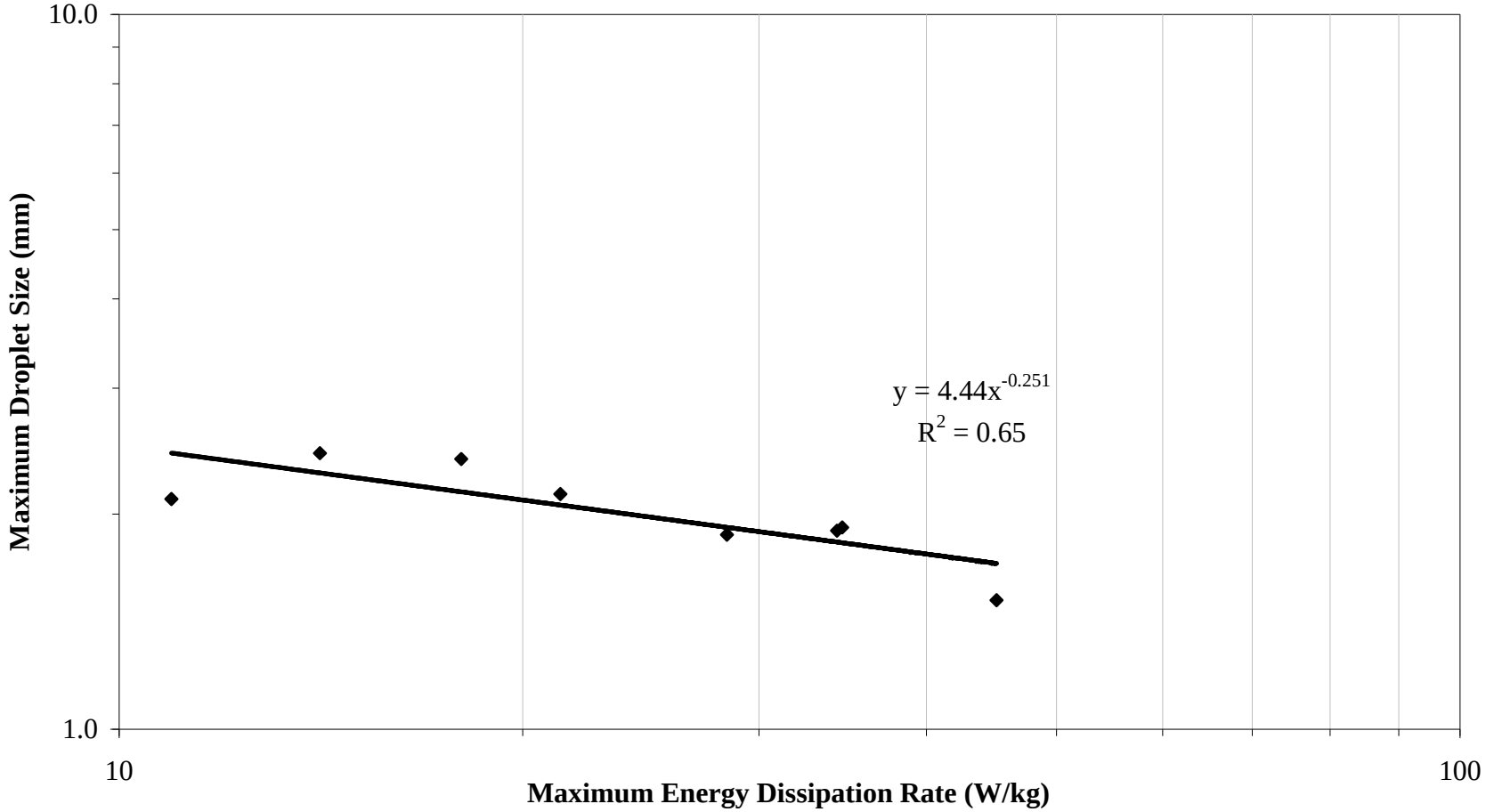

Figure 4.2 Maximum Droplet Size vs Maximim Energy Dissipation Rate for Bitumen/Toluene Blend

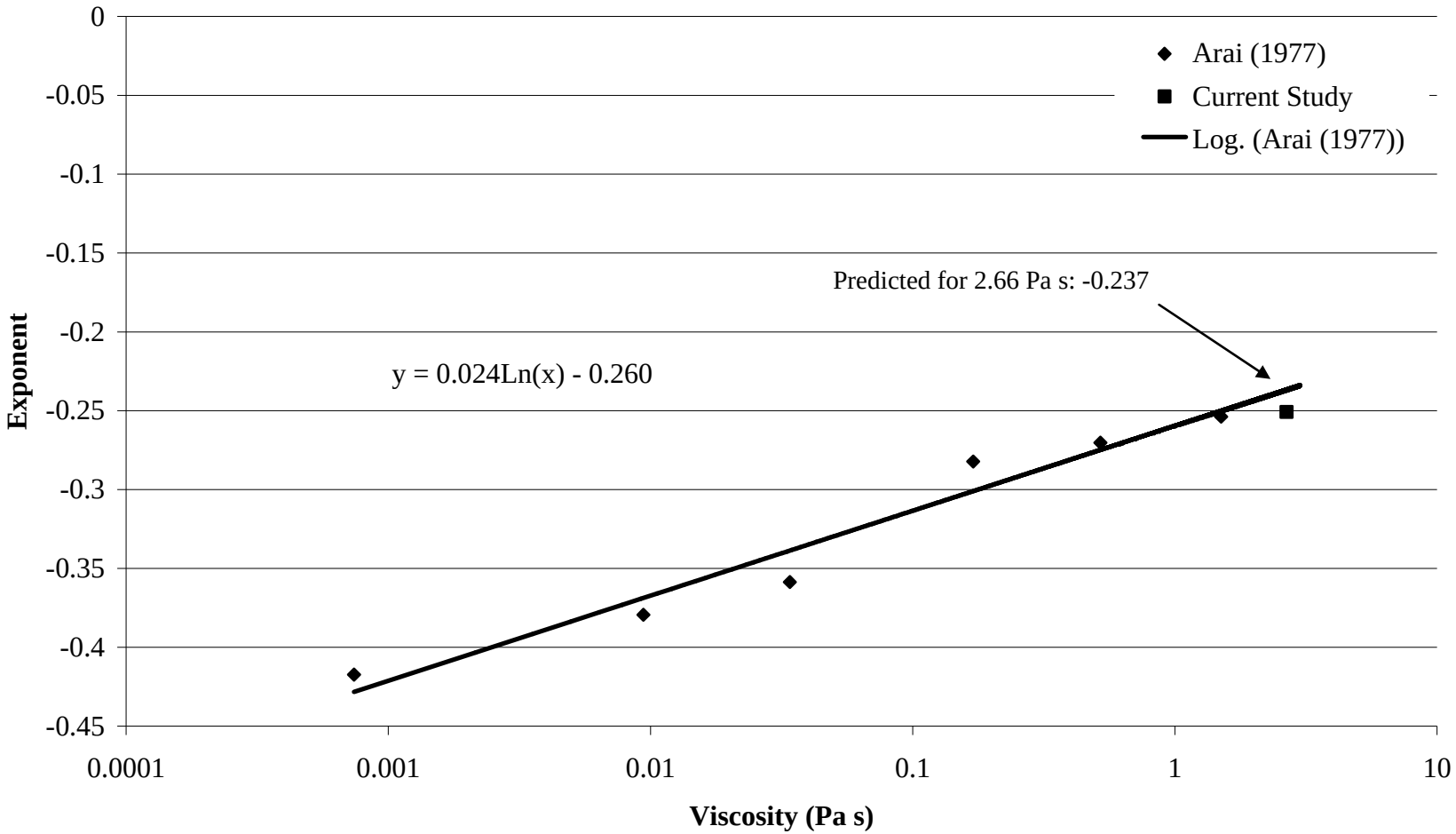

Figure 4.3:Comparison of Toluene Diluted Bitumen Power Law Exponent to Arai (1977)

4.2.3 Model Oil Discussion and Validation of Experimental Setup

The validation of the bitumen / toluene experimental results is based on the ability to reproduce literature trends and theoretical predictions. As illustrated above, the experimental results align well with literature values. In addition, the theoretical relationship derived between ε_{max} and d_{max} for viscosity-governed breakup was derived to give a power law exponent of -0.25 (in **Section 2.3.4**). Therefore, the difference between the theoretical power law exponent and the experimental value of –0.251 is negligible with a percent difference of 0.32%. Consequently, the setup is validated via two separate comparisons:

1) The power law exponent is within experimental error of the extrapolated Arai (1977) trend line, and
2) the relationship between d_{max} and ε_{max} mirrors the theoretically derived relationship from viscous breakup

4.3 Bitumen Experiments

Investigations into the effects of the rate of energy dissipation, ε, on the maximum droplet size, d_{max}, are important in a variety of industries where immiscible liquid-liquid mixing occurs. In the oil sands industry, it is generally acknowledged that larger bitumen droplets are recovered more easily than small droplets. Due to the highly viscous nature of bitumen, comparisons to other situations involving immiscible liquid dispersions are not available. This section of the study investigates the effect of different mechanical agitation devices (i.e. impellers) on d_{max}. Additionally, a relationship between ε_{max} and d_{max} will also be developed.

4.3.1 Effect of Varying Agitation Device

Two different impellers were used to investigate the effect of the agitation device used to dissipate energy into the system. A Rushton turbine and a hydrofoil (as specified in **Section 2.4.2)** were used. The maximum energy dissipation rates reported in this study were determined using the following equation, as developed by Zhou (1997);

$$\varepsilon_{\max} = 0.967 N^3 D^2 \quad \text{hydrofoil}$$

$$\varepsilon_{\max} = 12.14 N^3 D^2 \qquad \text{Rushton turbine}$$

The coefficients in each equation, 0.967 and 12.14, were selected based on similar tank geometries as a setup used by Zhou. A more detailed explanation regarding these equations can be found in **Section 2.2.4** while determination of the coefficients is detailed in **Section 3.5.2**. **Figure 4.4** shows how ε_{max} changes with impeller speed. As illustrated, at similar impeller rotational speeds, ε_{max} for the Rushton turbine is nearly an order of magnitude higher than the hydrofoil. For the hydrofoil, there is a restriction of the impeller speeds because as the pumping action of the hydrofoil becomes too great, air is entrained within the system and bitumen aeration results. Alternatively, low impeller speeds using the Rushton turbine (required to match the ε_{max} in the hydrofoil system) are typically inadequate to suspend the bitumen for extended periods of time.

Figure 4.5 is an illustration of d_{max} versus ε_{max} with data from both impellers. As can be seen, the data from the impellers overlap and a single trend line can be determined. Inserting a power law trend line, as is common when comparing these variables in liquid-liquid dispersions, an R^2 value of 0.85 is produced, thereby indicating a significant correlation. In addition, at an ε_{max} of ~ 47 W/kg, both impellers produced values of d_{max} within 0.1 mm of each other. These observations strongly indicate that ε_{max} is the controlling parameter in droplet breakup while the source of the energy dissipation is irrelevant.

4.3.2 Power Law Relationship

A power law exponent of -0.137 was produced by combining the data from the two impellers and fitting them with a single power law trend line. This trend line can be observed in **Figure 4.5**. The power law exponent obtained in this study, using highly viscous bitumen as the dispersed phase, was 45% lower than derived in theory (-0.25 as seen in **Section 2.3.4**). This study can also be

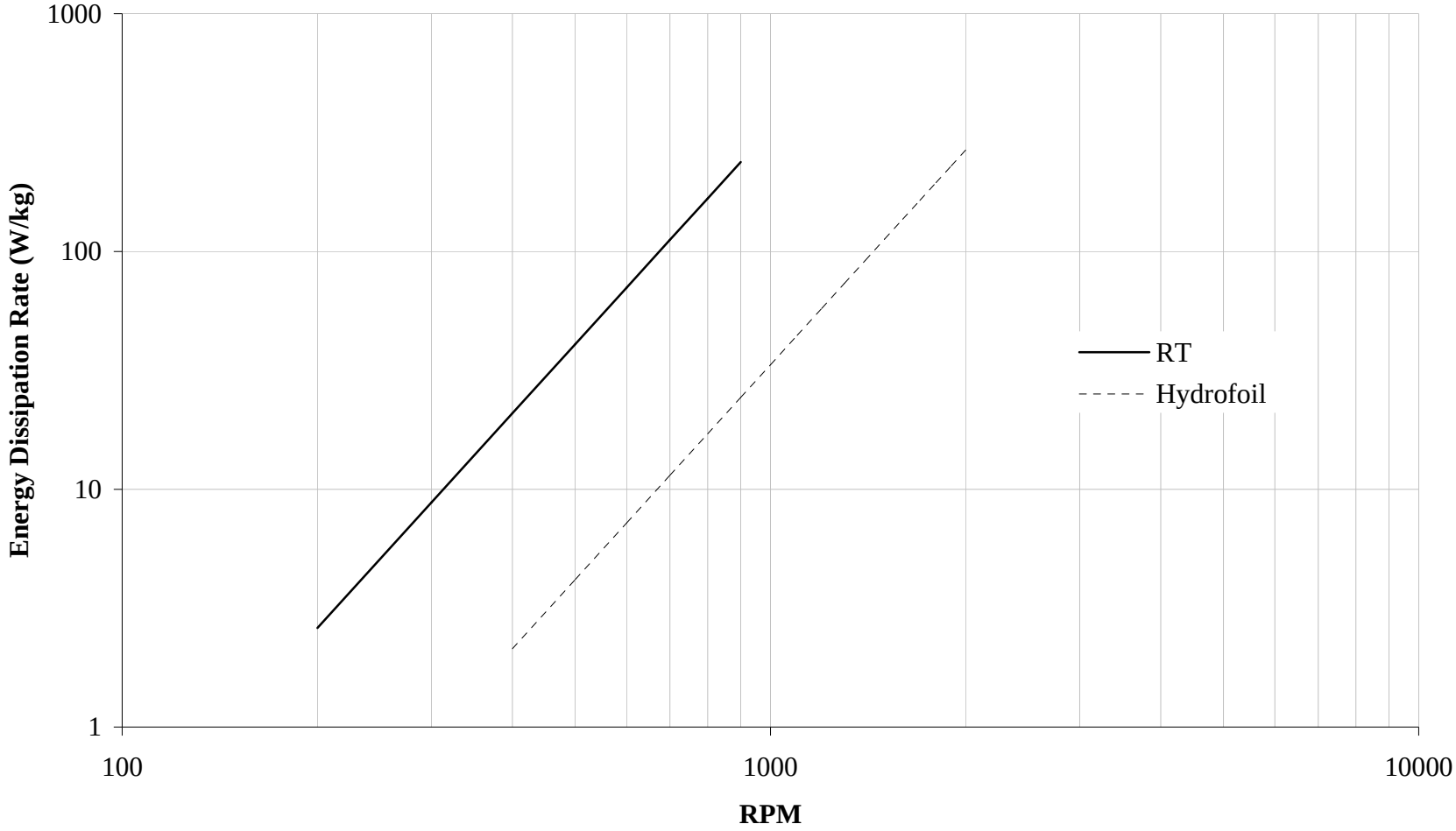

Figure 4.4 Energy Dissipation Rate vs RPM

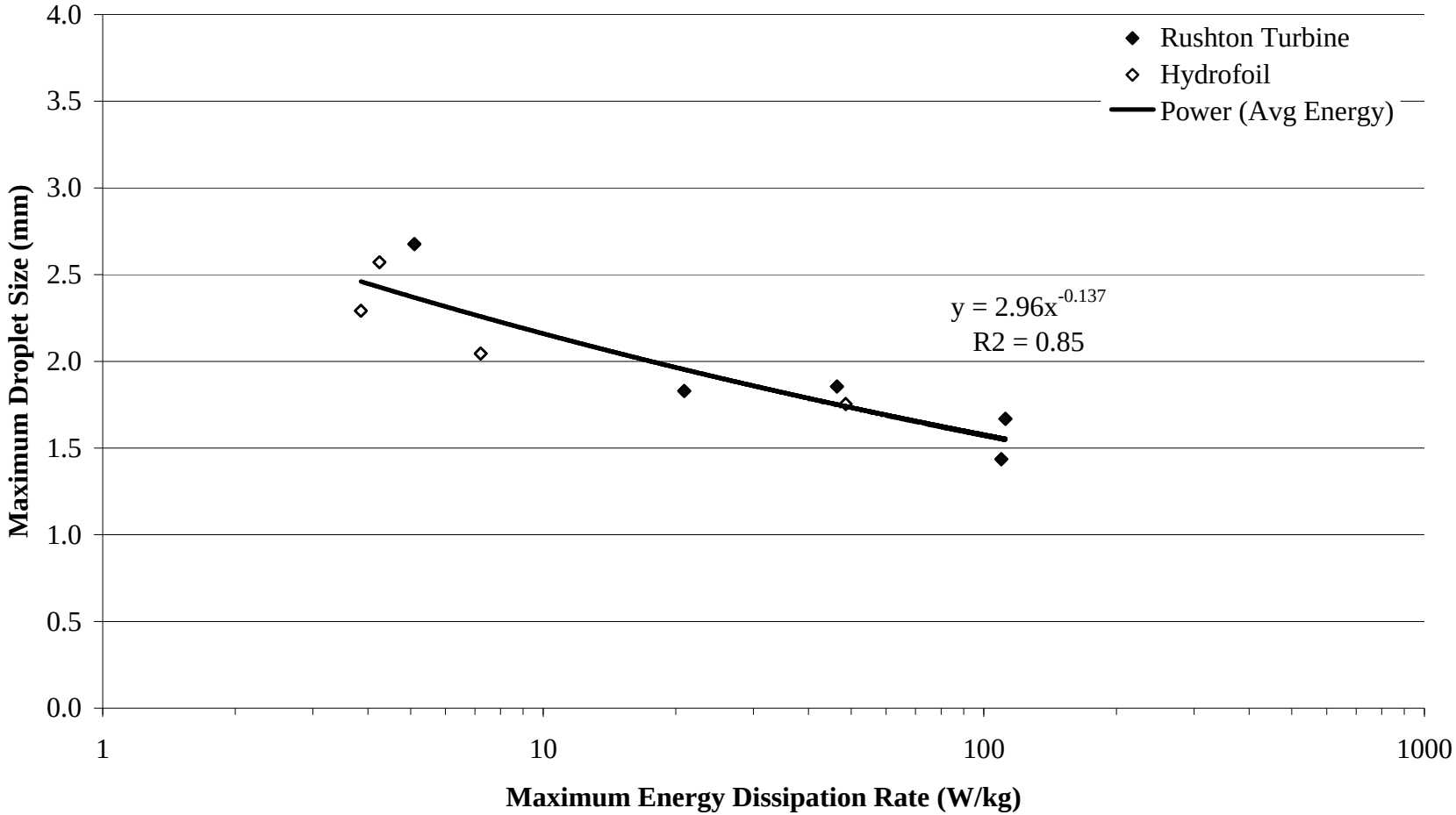

Figure 4.5 Maximum Droplet Size vs Maximum Energy Dissipation Rate for ATB

compared to data from Arai (1977). **Figure 4.6** shows the data of Arai along with an extrapolation of the trend line from 1.5 Pa·s to 22 Pa·s. From this data, a power law exponent of -0.19 is expected for 21.5 Pa·s bitumen. Again, a significant difference (28%) exists between this study's value and the extrapolation from Arai's work.

4.4 Analysis of Potential Errors

Several factors may have contributed to the difference between the aforementioned observations. The following section will document and analyze three of these factors.

4.4.1 Error in ε_{max} Calculation Related to Power Law Relationship Deviation

One source of this difference may be attributed to the estimation of the constant, c, when calculating the maximum energy dissipation rate, i.e.

$$\varepsilon_{\max} = cN^3D^2$$

where c is 0.967 for the hydrofoil and 12.14 for the Rushton Turbine.

As shown in **Section 3.3.2**, there is a significant difference between the literature power numbers and those determined in this study. As discussed previously, the power number is an indication of the ability to dissipate energy into the system, and does not indicate the local energy dissipation at any point with the system. The current setup, using a dished head, enables increased circulation rates when compared to flat bottomed tanks. Therefore, the total energy input into the system, and possibly the power number, may be less due to the improved circulation in the tank. However, Zhou (1998) determined that local isotropy existed in a variety of geometries, irrespective of the circulation rates within the tank. This result indicates that in order for the constant to change, the root mean square (rms) of the fluctuating velocities must also vary. Because these

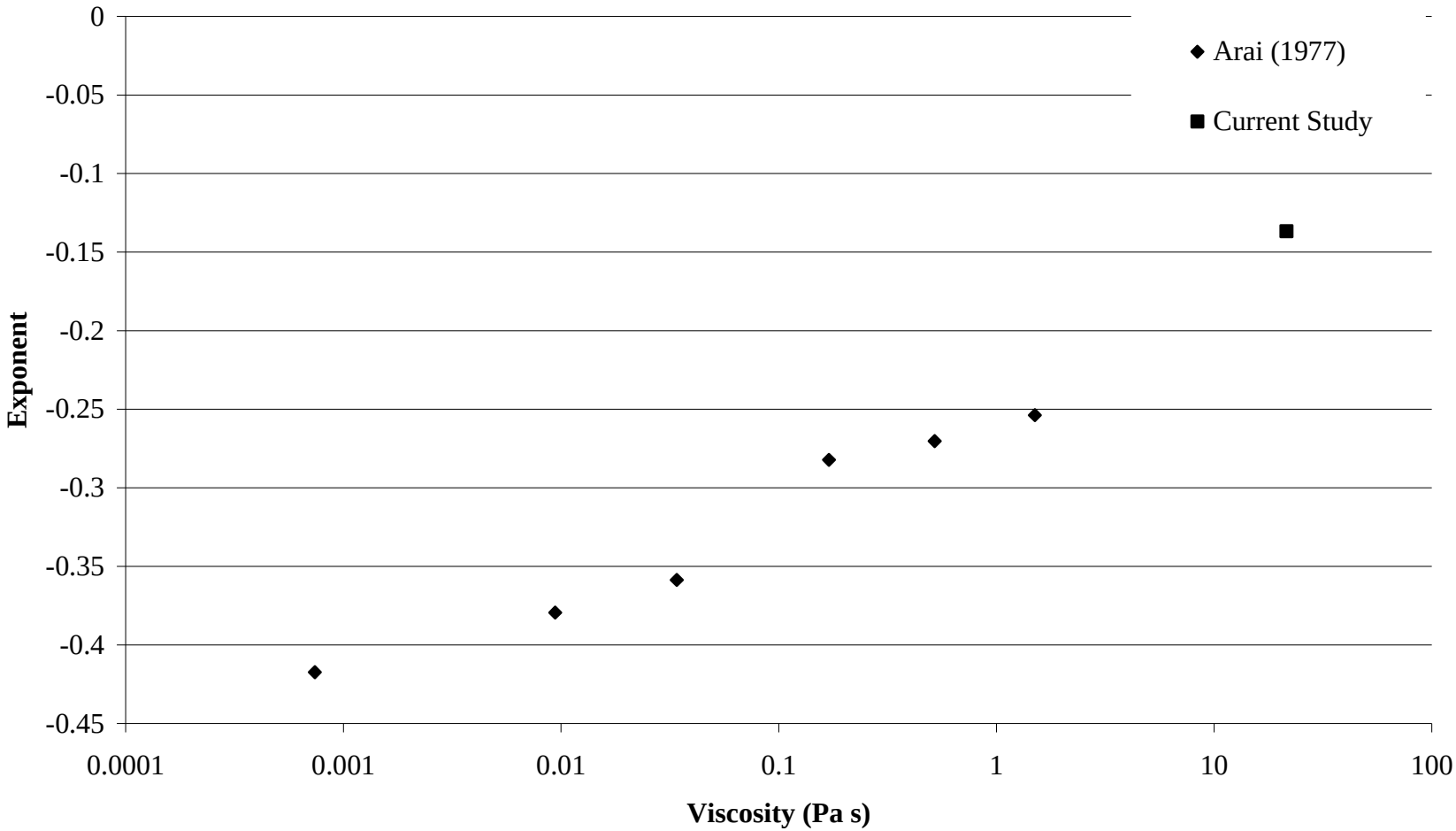

Figure 4.6:Comparison of Atmospheric Topped Bitumen Power Law Exponent to Arai (1977)

velocities are indeterminable in the current setup, it is not known how much the constant c will change for the impellers.

The actual constant c may be different than that used to determine ε_{max} in this study. If only one mixing device had been used in this experiment, the power law exponent would have been unaffected by an error in the value of the constant, c, used. However, with two mixers (the hydrofoil and the Rushton turbine) used in the determination of d_{max} vs ε_{max}, the values of 'c' both needed to both be indicative of the geometry of the current system. **Table 4.1** illustrates the percent error between the power law exponent found using the constants 0.967 and 12.14 for the hydrofoil and the Rushton turbine, respectively, and those found by altering the constant c. It can be seen that changing the constants in each equation by the same factor leaves the power law exponent unaltered as expected (both reflect the geometry of the mixing system). It is only when the constants change by a differing amount that errors begin to arise. The errors are relatively small with only an 11% difference occurred when changing the Rushton turbine constant by -20% and the hydrofoil by +20% (a net 40% difference). Therefore, errors in the calculation of ε_{max} and the power law exponent may have been caused by inaccuracies when estimating the constant, c.

Table 4.1 - Power Law Exponent Error as a Result of Rushton Turbine and Hydrofoil Constant Error

		Error in Rushton turbine constant, c, in $e_{max}=cN^3D^2$					
		-20%	**10%**	**0%**	**5%**	**10%**	**20%**
Error in hydrofoil constant, c, in: $e_{max}=cN^3D^2$	**-20%**	0%	-3%	-6%	-7%	-8%	-11%
	-10%	3%	0%	-3%	-4%	-5%	-8%
	-5%	4%	1%	-1%	-3%	-4%	-6%
	0%	5%	3%	0%	-1%	-2%	-5%
	5%	7%	4%	1%	0%	-1%	-4%
	10%	8%	5%	2%	1%	0%	-2%
	20%	9%	7%	4%	3%	2%	0%

4.4.2 Effect of Viscosity Variation on Power Law Relationship

Slight variations in temperature can cause large deviations in viscosity, as illustrated in **Figure 3.12**. A temperature profile of a common experiment can be seen in **Figure 4.7**. Although a small variation of temperature within the experiment is observed, the steady state temperature between experiments varied between 49°C and 51°C. Over this range of temperature, the viscosity varies by 19% which could have caused error within the experiment. However, each experiment had extremely similar temperature profiles as illustrated in **Figure 4.7**. Therefore, the variance of temperature within the experiment may have introduced a small amount of error to the results however due to the consistent way the temperature varied, this error is minimal.

4.4.3 Effects of Water Chemistry on Experimental Power Law Relationship

Another source of error may have been the water chemistry of the continuous fluid. During experimentation, the simulated process water (SPW), used as the continuous fluid, may have contained a variety of impurities that affected the bitumen droplet sizes.

Polyvalent ions are one type of impurity that would have affected the maximum droplet size. As discussed in **Section 3.3.2**, polyvalent ions such as Calcium (Ca^{2+}) and Magnesium (Mg^{2+}) compress the electrical double layer and cause the coalescence efficiency to increase dramatically (Moran, 2005). By increasing the rate of coalescence, the maximum droplet size within the tank may also increase. Ultimately, however the effects of water chemistry likely did not have an influence on d_{max} due to the extremely low concentrations used.

4.4.4 Effect of Viscosity on ε_{max}

A brief investigation into the effect of bitumen viscosity on d_{max} was performed. In these experiments, the water temperature was varied. An impeller speed of 400 rpm was used for all seven experiments. **Figure 4.8** illustrates the values of d_{max} obtained at various bitumen viscosities (adjusted via temperature).

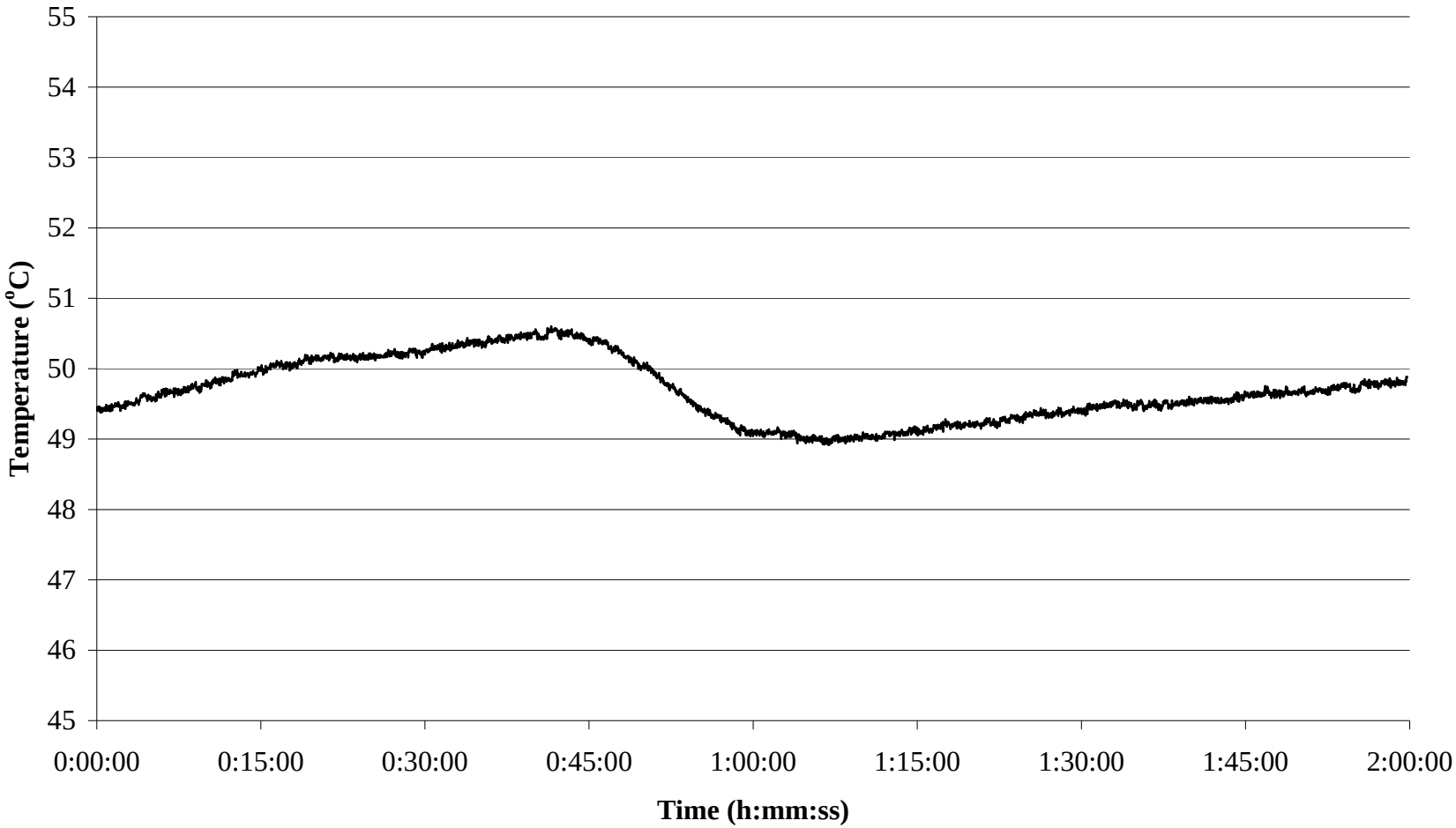

Figure 4.7 Temperature Variation during Experiment

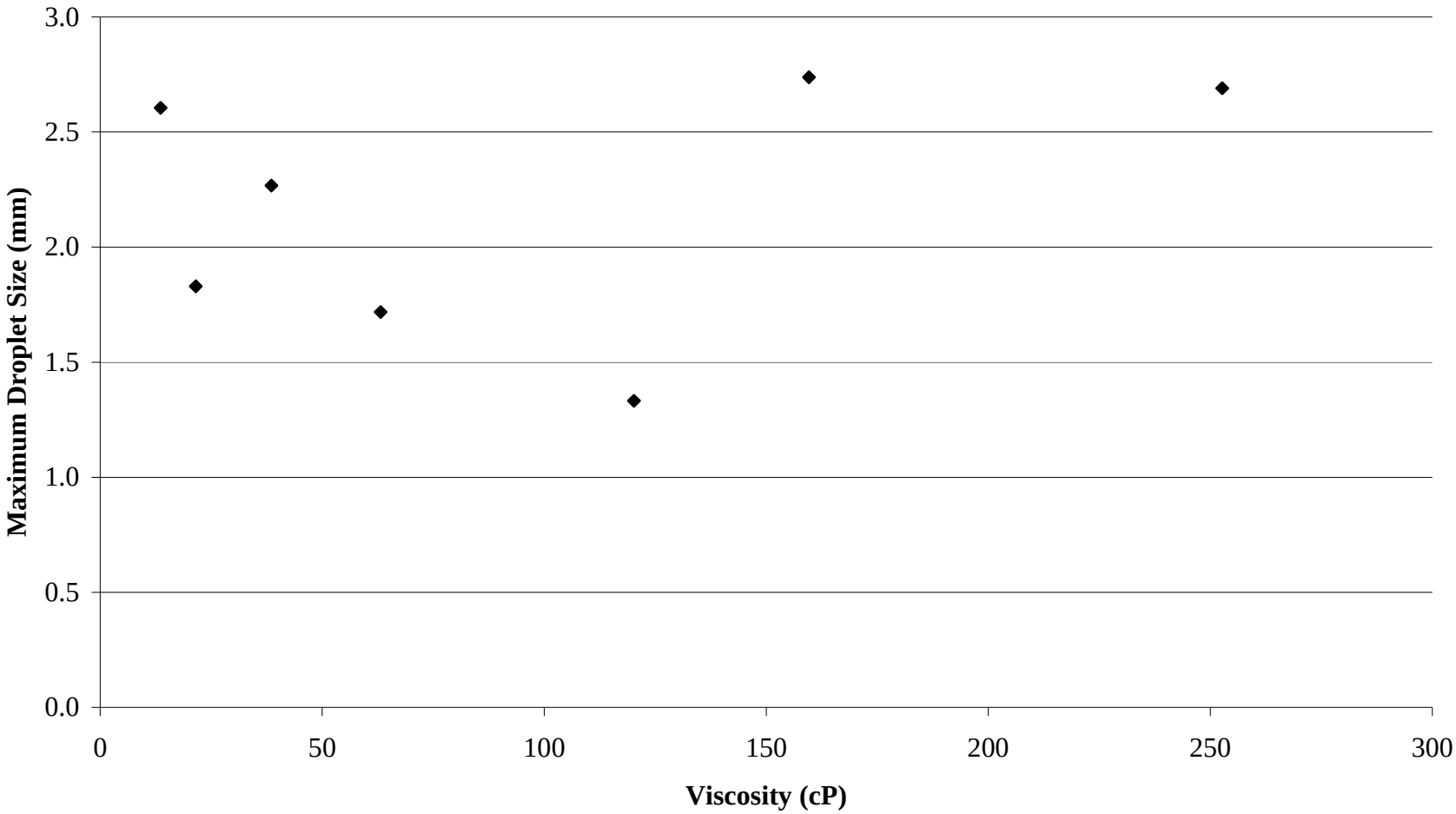

Figure 4.8 Maximum Droplet Size vs Bitumen Viscosity

The figure shows no observable trends. However, if the two highest viscosity experiments are neglected, the droplet size decreases as the viscosity is increased.

One source of error in determining this factor was in the addition of the bitumen. Due to the 10-fold increase in viscosity, the manner in which bitumen was added had to be altered. In all cases, a spoon was used to drop the bitumen in; at warmer temperatures (hence lower viscosities), the bitumen flowed off the spoon into the impeller. In cold water (hence higher viscosities), the bitumen came off the spoon in larger globules. In addition, adhesion of bitumen to the tank wall was more prevalent at colder temperatures. Therefore, bitumen addition techniques should perhaps be altered for future viscosity vs d_{max} research.

4.5 Conclusions

The experimental apparatus performed as expected when investigating the relationship between d_{max} and ε_{max} for the 2.66 Pa·s toluene/bitumen system. A power law exponent of –0.25 was discovered for this dispersion which is very similar to the theoretical value of –0.25 and the Arai (1977) extrapolation of -0.236. Therefore, the system was shown to be valid for the investigation of moderately viscous dispersions.

The type of impeller was found to be irrelevant when investigating the d_{max} (at a constant ε_{max}). A power law exponent of -0.137 was obtained for the 21 Pa·s bitumen system and was seen to be significantly smaller than the theoretical value of -0.25 and the extrapolated value of -0.19 from Arai (1977). Several sources of error may have been present in the study, such as assumption of the constant c (in equation (2-21)), water temperature, and water chemistry.

Chapter 5
Conclusions and Recommendations

5.1 Introduction

This study had the following objectives:

1) Design and calibrate an experimental device capable of creating a liquid-liquid dispersion and measuring the drop sizes in-situ
2) Develop a relationship between the maximum droplet size, d_{max}, and maximum energy dissipation rate, ε_{max}, for a bitumen-water dispersion

This chapter will evaluate the successes and failures involved in meeting each of these objectives. In addition, recommendations for future work will also be made.

5.2 Objective 1: Experimental Design and Calibration

The experimental design was described in **Chapter 3**, based upon the literature findings outlined in **Chapter 2**. The biggest difference between this study's experimental apparatus and those found in literature is the geometry of the tank bottom. In the literature, typically a flat bottom tank is used. However, in order to achieve suspension of solid particles in future work, an ASME Dished head was used. This may have contributed to the low power number obtained using a Rushton turbine due to increased circulation. This modification did not have a significant effect on the power law relationship between ε_{max} and d_{max} for the toluene/bitumen experiment. The experimental results agreed both with theory and extrapolated data from another investigator (Arai, 1977). Therefore, the experimental apparatus and procedure were deemed to be validated.

To more accurately determine the ε_{max} and the droplet size distribution, a glass tank should have been implemented such that a Laser Doppler Anemometer (LDA) could be utilized. Determining the maximum root mean square (rms) of the fluctuating velocities would have improved the estimation of ε_{max} experienced by the droplets. In addition, an LDA would have been able to identify much smaller droplets than the DaVis 6 software. It also could have produced a droplet

size distribution for transparent oil, thereby allowing a much less viscous model oil to be analyzed and compared to literature values.

5.3 Objective 2: d_{max} vs ε_{max} Relationship

The bitumen experiments produced a relationship between ε_{max} and d_{max} of:

$$\varepsilon_{\max} = constant \times d_{\max}^{-0.1367}$$

According to theory, a dispersed phase where viscosity is the primary restorative factor should have a power law exponent of -0.25. However, the viscosities of fluids investigated in the literature are nearly an order of magnitude smaller than the 21 Pa·s bitumen used in the current study, thereby requiring excessive extrapolation. Additionally, extrapolating data from Arai (1977) resulted in an exponent of -0.19. Therefore, Arai's result deviates from the theoretical value of -0.25 and indicates a decreasing power law exponent as viscosity increases. It should be noted that Arai's data was extrapolated by nearly an order of magnitude, from ~ 2 Pa·s to 21.5 Pa·s. Therefore, the accuracy of his extrapolation is questionable. Some sources of error in the current work may be attributed to factors such as the constants used in the calculation of the maximum dissipation rate, the exponential relationship between bitumen viscosity and temperature, and the impure nature of bitumen.

5.4 Future Work

At the conclusion of this research, several areas for future work are evident. One such area is a further analysis into the power law exponent calculated for the high viscosity Atmospheric Topped Bitumen. Calculation of power law exponents for toluene-bitumen blends ranging in viscosity between the 2.7 Pa·s model oil and the 21.5 Pa·s bitumen investigated in this study may indicate how the exponent changes as the viscosity is increased. Achieving this

objective may provide insight into why the power law exponent increases beyond the theoretically predicted value of -0.25 may become evident.

In addition, a study of bitumen droplet breakup in the non-viscosity dominated breakup regime (i.e. for viscosities less than 1.5 Pas) would be valuable. This data could be used to plot how the power law exponent changes with respect to viscosity and subsequently used to compare with viscosity standards (e.g. the data could be plotted on Figure 4.3 to serve as a direct comparison). This study would provide more information on the nature of bitumen droplet breakup and serve as a tool for comparing bitumen droplet versus viscosity standard droplet breakup.

Appendix

Illustration of Sample Droplet Size Calculation

The procedure for the calculation of the Bitumen Droplet Size can be found in **Section 3.5.2**. The following is an example of a sample experiments for a hydrofoil operating at 503 rpm.

The first stage of the experiment was converting the video into a series of photographs that could be analyzed using the DaVis 6 software. An example of a photo that was analyzed can be seen in **Figure A.1**. Each 20 second video segment was used to created 20 photographs similar to **Figure A.1**. DaVis 6 was used to analyze the size of the bitumen droplets for all 100 photographs. An abbreviated example of these results can be seen in **Table A.1**. From this Table, the maximum droplet size is documented.

Table A.1 is the results from the video analyzed at 120 mins. The maximum droplet size is taken from the remaining times (2, 4, 8, 12, 20, 30, 40, 60, 80, 100, and 120 mins). These maximum droplet sizes are plotted (**Figure A.2**) and a determination of the equilibrium droplet time is made. The droplet sizes after this equilibrium droplet time are averaged. This final droplet size is the maximum droplet size for the specified rpm / energy dissipation rate of this impeller.

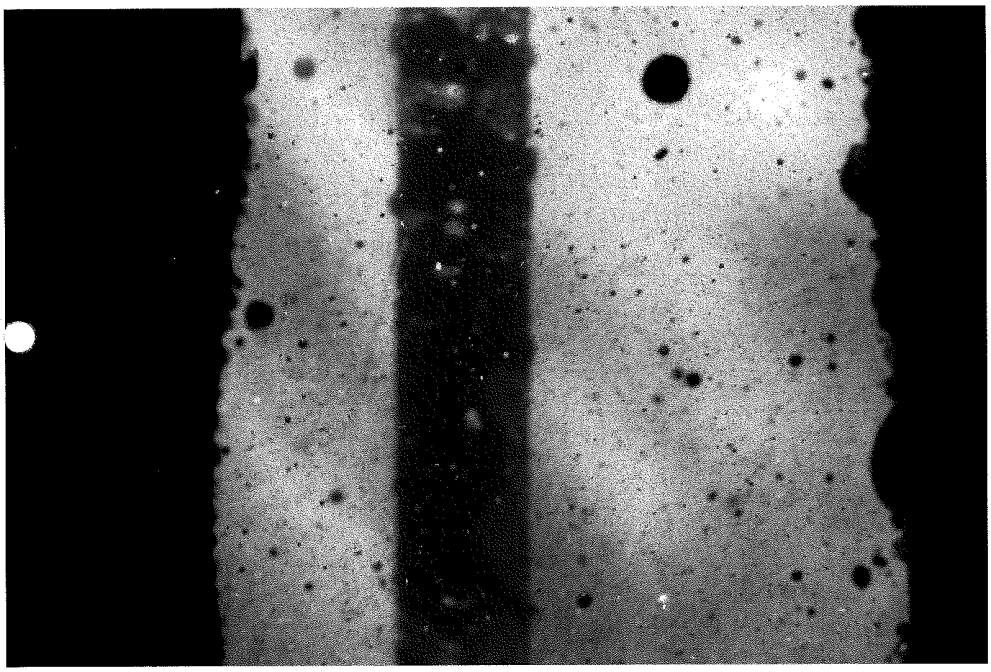

Figure A.1: Example Photograph for Analysis by DaVis

Table A.1: Illustration of DaVis Software Output

Analyzed Particles = 3541		
statistical number of Particles = 3683.37		
Mean Diameter(D10) = 10.6487 pixel	10.6487	0.450179906
RMS = 5.18335	5.18335	0.219129097
Sauter Mean Diameter (D32) = 18.7006 pixel	18.7006	0.790578601
D[V,10] = 8.60119 pixel	8.60119	0.363620245
D[V,50] = 20.8301 pixel	20.8301	0.880604436
D[V,90] = 57.1793 pixel	57.1793	2.417287735

Scaling: x' = 1 * x 0.0422756

Diameter High Threshold: Diameter of High Threshold (High Level, Second Segmentation)

Diameter Low Threshold: Diameter of Low Threshold (Low Level, Second Segmentation)

Average Diameter: Average Diameter of High and Low Threshold

Note: The following values are all given in Pixels

Diameter High Threshold	Diameter Low Threshold	Number of Pixel Low Threshold	Number of Pixel Low Threshold	Average Diameter	Scaled Diameter
7.74	8.14	47	52	7.94	0.3355
10.40	11.06	85	96	10.73	0.4536
7.48	7.90	44	49	7.69	0.3252
8.59	8.81	58	61	8.70	0.3679
6.96	7.14	38	40	7.05	0.2979
9.10	9.64	65	73	9.37	0.3961
6.38	7.23	32	41	6.80	0.2876
13.96	14.71	153	170	14.33	0.6060
13.35	14.27	140	160	13.81	0.5839
8.59	8.96	58	63	8.77	0.3710
14.00	15.18	154	181	14.59	0.6169
12.15	12.46	116	122	12.31	0.5203
10.59	11.34	88	101	10.96	0.4635
10.22	10.59	82	88	10.40	0.4397
13.73	14.32	148	161	14.02	0.5928
5.75	6.08	26	29	5.92	0.2501
6.77	7.05	36	39	6.91	0.2921
12.05	12.77	114	128	12.41	0.5245
9.37	9.84	69	76	9.61	0.4061
12.46	12.96	122	132	12.71	0.5375
7.65	8.14	46	52	7.89	0.3338

Diameter High Threshold	Diameter Low Threshold	Number of Pixel Low Threshold	Number of Pixel Low Threshold	Average Diameter	Scaled Diameter
12.91	13.49	131	143	13.20	0.5582
7.90	7.98	49	50	7.94	0.3356
7.14	7.40	40	43	7.27	0.3073
7.14	7.48	40	44	7.31	0.3091
12.87	13.59	130	145	13.23	0.5592
15.26	16.31	183	209	15.79	0.6675
6.86	7.23	37	41	7.04	0.2978
9.30	9.97	68	78	9.64	0.4073
13.87	14.45	151	164	14.16	0.5985
8.37	8.88	55	62	8.63	0.3647
11.62	12.26	106	118	11.94	0.5047
7.48	7.90	44	49	7.69	0.3252
17.26	18.19	234	260	17.73	0.7494
13.21	14.00	137	154	13.61	0.5752
6.77	6.96	36	38	6.86	0.2901
10.16	10.70	81	90	10.43	0.4409
14.93	15.96	175	200	15.44	0.6528
57.99	59.55	2641	2785	58.77	2.4845
6.58	6.96	34	38	6.77	0.2861
6.58	6.86	34	37	6.72	0.2842
10.59	11.23	88	99	10.91	0.4611
11.56	12.31	105	119	11.94	0.5046
12.41	13.21	121	137	12.81	0.5415
10.40	10.76	85	91	10.58	0.4474
10.88	11.94	93	112	11.41	0.4824
7.14	7.82	40	48	7.48	0.3161
9.97	10.88	78	93	10.42	0.4407
8.29	8.67	54	59	8.48	0.3585
13.45	14.00	142	154	13.72	0.5802
7.40	7.74	43	47	7.57	0.3199
6.38	6.68	32	35	6.53	0.2760
14.36	15.39	162	186	14.88	0.6289
6.38	6.77	32	36	6.58	0.2780
11.67	12.31	107	119	11.99	0.5069
9.71	10.28	74	83	9.99	0.4225
7.14	7.57	40	45	7.35	0.3109
10.09	10.65	80	89	10.37	0.4383
13.45	14.23	142	159	13.84	0.5850
9.84	10.52	76	87	10.18	0.4304
7.57	7.82	45	48	7.69	0.3252
7.31	7.40	42	43	7.36	0.3110
6.68	7.14	35	40	6.91	0.2920
9.84	10.40	76	85	10.12	0.4278
7.90	8.37	49	55	8.13	0.3438

NOTE - Another 58 pages of Sizing was performed but NOT included in the APPENDIX

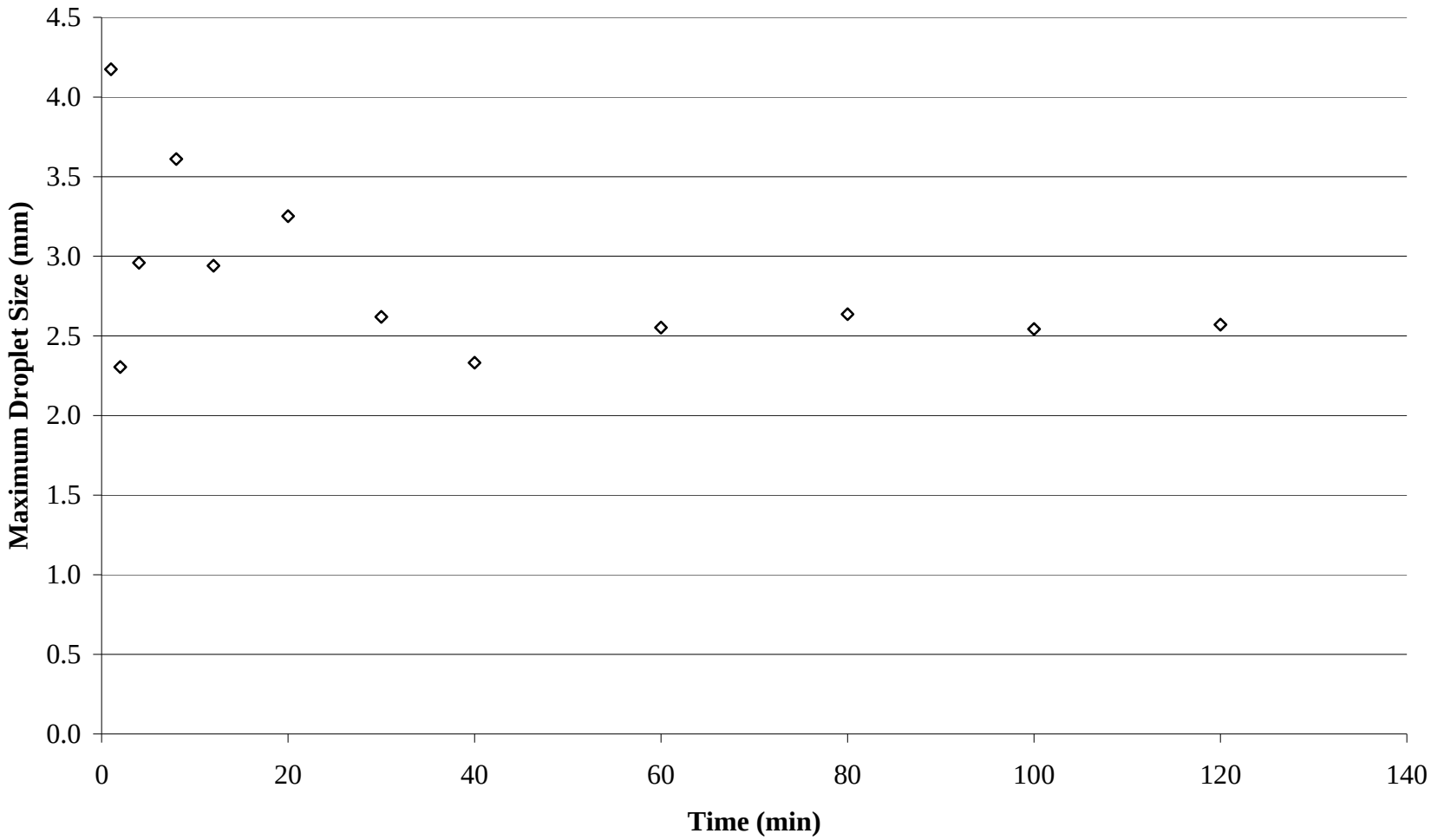

Figure A.2: Maximum Droplet Size vs Time for Hydrofoil @ 503 RPM